ACSNANO

www.acsnano.org

ARTICLE

Reverse Actuation of Polyelectrolyte Effect for *In Vivo* Antifouling

Woojin Choi, Sohyeon Park, Jae-Sung Kwon, Eun-Young Jang, Ji-Yeong Kim, Jiwoong Heo, YoungDeok Hwang, Byeong-Su Kim, Ji-Hoi Moon, Sungwon Jung, Sung-Hwan Choi,* Hwankyu Lee,* Hyo-Won Ahn,* and Jinkee Hong*

Cite This: *ACS Nano* 2021, 15, 6811−6828

Read Online

ACCESS | Metrics & More | Article Recommendations | Supporting Information

ABSTRACT: **Zwitterionic polymers have extraordinary properties, that is, significant hydration and the so-called antipolyelectrolyte effect, which make them suitable for biomedical applications. The hydration induces an antifouling effect, and this has been investigated significantly. The antipolyelectrolyte effect refers to the extraordinary ion-responsive behavior of particular polymers that swell and hydrate considerably in physiological solutions. This actuation begins to attract attention to achieve *in vivo* antifouling that is challenging for general polyelectrolytes. In this study, we established the sophisticated cornerstone of the antipolyelectrolyte effect in detail, including (i) the essential parameters, (ii) experimental verifications, and (iii) effect of improving antifouling performance. First, we find that both osmotic force and charge screening are essential factors. Second, we identify the antipolyelectrolyte effect by visualizing the swelling and hydration dynamics. Finally, we verify that the antifouling performance can be enhanced by exploiting the antipolyelectrolyte effect and report reduction of 85% and 80% in *ex* and *in vivo* biofilm formation, respectively.**

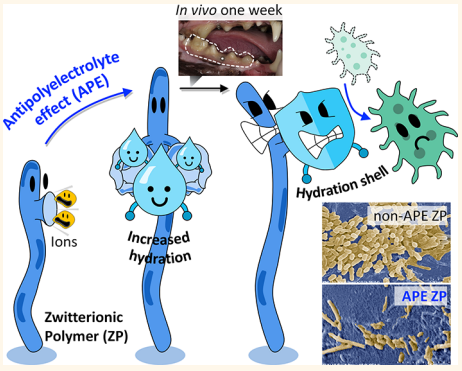

KEYWORDS: *zwitterionic polymer, in vivo antifouling, antipolyelectrolyte effect, implantable biomedical device, polymer science*

An *in vivo* infection caused by implanted medical devices can be fatal and is a reasonably frequent occurrence, for example, in European hospitals, approximately 4.1 M patients acquire infections caused by defective devices each year.[1] Besides, microorganisms such as SARS-CoV-2 can remain viable on the surfaces of engineering plastics for more than 72 h, enabling transmission through objects (such as parcel services).[2] Therefore, sophisticated antifouling materials are required. Recent studies on typical lab-scale antifouling polymers, poly(ethylene glycol) (PEG),[3] have a problem when they are used *in vivo*, that is, the ether groups, the originality of PEG's antifouling, and cleavage under the biological environment (*e.g.*, oxidations due to pH or enzyme).[4,5] The use of zwitterionic polymers (ZPs) is a potential alternative to PEGylation owing to their better hydration ability.[6−8] For example, unit sulfobetaine functional groups could tightly bind with eight water molecules. Considering the volumetric property, sulfobetaine methacrylate (SBMA) could hydrate *ca.* 3.5−5.5 times that of PEG.[9] In particular, the hydration shell formed by ZPs acts as an energy barrier because it induces entropy loss during nonspecific adsorption.[10]

Another extraordinary characteristic of ZPs, the antipolyelectrolyte effect (APE), is beginning to attract attention.[11,12] As suggested by the nomenclature, APE is the opposite of the "polyelectrolyte effect" (Figure 1a). In detail, APE refers to the phenomenon in which inter- and intrapolymer interactions are weakened, resulting in swelling and considerable hydration at high ionic strengths (Figure 1b).[13] State-of-the-art APE research has engineered the friction coefficients of the polymer brush,[11,14] volumetric variations of the hydrogel,[12,15] and *in vitro* antifouling of the polymer.[16] Further, APE actuation could be exploited *in vivo* to achieve an enhanced antifouling effect because body fluids are rich in ions. Thus, APE is a promising approach to increase the intrinsic functions of polymers *in vivo*, especially considering that polymers generally lose their functions under physiological conditions (*e.g.*, the ether groups of PEG).[4,5]

APE is not available in all ZPs, for example, APE is not possible for (2-methacryloyloxyethyl phosphorylcholine (MPC)),[17,18] however possible for SBMA and carboxybe-

Received: December 13, 2020
Accepted: March 18, 2021
Published: March 26, 2021

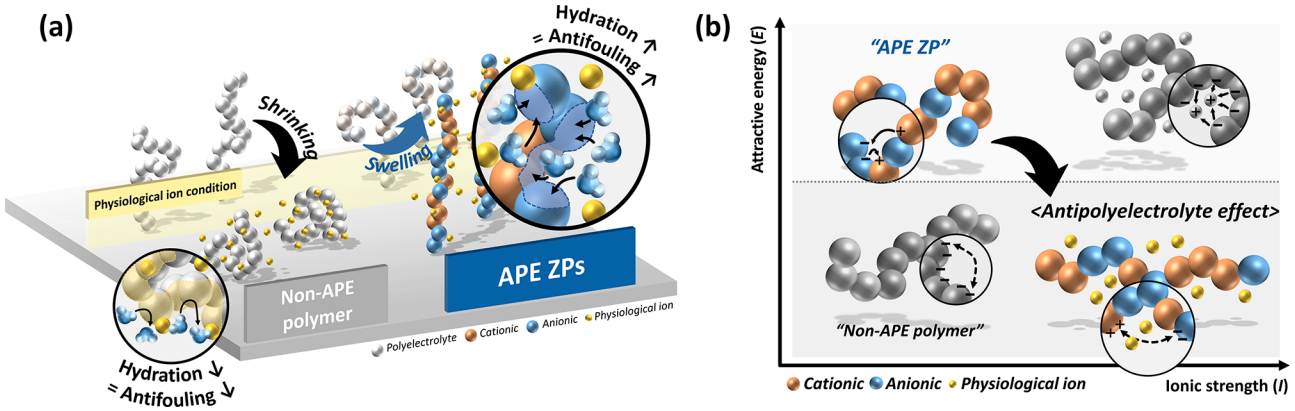

Figure 1. Schematic illustrations of (a) the extraordinary ion-responsible behavior of ZPs, exhibiting the APE. The gray spheres on the left present the polymer with no APE (so-called, non-APE polymer). On the other hand, the blue (anionic moiety) and orange-red (cationic moiety) spheres on the right represent the ZPs exhibiting APE (so-called, APE ZPs). Since the ions positively influenced the APE, the ions were illustrated as yellow spheres or a wall. Then, the impact of APE on the enhanced hydration and antifouling performance was summarized as a circle inserted in the scheme. (b) Difference between the polyelectrolyte effect and APE as the function of ionic strength (*x*-axis) and attractive energy (*y*-axis).

taine.[13,19] The reason why the different actuations of representative ZPs occurred is still unclear. Thus, the deficient understanding of the factors regulating APE is one of the primary hurdles preventing its futuristic applications.

Therefore, we established the sophisticated cornerstone of APE by solving the question, why the behaviors of MPC and SBMA are disparate. In detail, we have investigated the APE-determining thermodynamic parameters and conducted experimental verifications. First, we identified two essential factors required for the APE: osmotic force[20] and charge screening effect.[21] Second, we conducted an in-depth verification process to determine whether the synthesized ZPs exhibit APE or not. Finally, we identified ZP with optimal antifouling performance after exposure to various microorganisms. Here, we refer to specific ZPs exhibiting APE as APE ZPs and nonexhibiting APE as non-APE ZPs.

Consequently, the APE actuation system was found to exhibit outstanding antifouling performance. Interestingly, the ultralow fouling of nonspecific protein adsorption (<5.0 ng cm^{-2}) was achieved under physiological conditions.[13] Further, the APE ZPs exhibited exceptional antifouling effects in four fouling models: (i) *in vitro* protein adsorption: *ca.* 91%, (ii) *in vitro* bacterial adhesion: *ca.* 80%, (iii) *ex vivo* biofilm formation: *ca.* 85%, and (iv) *in vivo* biofilm formation: *ca.* 80% reduction (the latter is a realistic but extreme biofouling model). Crucially, our APE-based antifouling ZPs remains functional for up to 3 days in a dynamic oral environment, suggesting that it could be used in other parts of the human body.

RESULTS AND DISCUSSION

Design and Optimization of the Surface Modification with ZPs. In this study, a surface-initiated activator regenerated by electron-transfer atom-transfer radical polymerization (SI-ARGET ATRP) was used. This allowed us to simultaneously achieve high functionalization density (*i.e.*, grafting density) under moderate reaction conditions. Figure S1 presents a detailed schematic of the surface modification process. In the "*graft from*" approach, the monomers are tethered to the substrate sequentially. Further, to minimize the probability of chain termination, we used living polymerization. Technically, the rate of chain initiation dominates the other steps, such as propagation and termination.[22] Surface-initiated atom-transfer radical polymerization (SI-ATRP) is the representative living polymerization method of the various "*graft from*" approaches. We also utilized an additional reducing agent to allow polymerization under ambient conditions, that is, SI-ARGET ATRP. Thus, we could efficiently regulate the molecular characteristic of ZPs *via* SI-ARGET ATRP (Figure S1).

The SI-ARGET ATRP system involves two main steps: (i) immobilization of the initiators and (ii) polymer brush growth. The efficiency of the first step, which affects the density of the surface-immobilized initiators, directly controls the grafting density and degree of surface functionalization. Thus, we optimized the first step to maximize ATRP initiator immobilization (Figure S2). In the second step, we aimed to increase the surface modification efficiency. Here, ZPs are denoted as (*X*)MPC/(*Y*)SBMA, where *X* and *Y* are the mole fractions of the monomers in the copolymer.

First, we established the optimized ATRP initiator immobilization condition. Figure S2a summarizes the processes for the synthesis and immobilization of the catecholic ATRP initiators. The naturally occurring catecholamine, dopamine, was used because of its adhesivity on various substrates. We assumed two conformations of the tethered initiators reflecting the self-polymerization of the residual dopamine (Figure S2b).[23] The surface-immobilized dopaminechrome, a representative derivative of self-polymerization (Figure S2c),[24] might be abundant within the formation of undesired conformations and could reduce the grafting density.

We double-checked the optimal immobilization time when the desired initiator conformation was maximized. First, we conducted Raman spectroscopy measurements for immobilization times from 10 min to 24 h (Figure S2d). In detail, we tracked the carbonyl group at near 1600 cm^{-1}, which is only present in dopamine and not in dopaminechrome. No significant carbonyl peak was observed in the spectra in the initial stages of reaction, but this band appeared after 3 h of immobilization. Because the formation of undesired conformation also increased with an increase in immobilization time, we evaluated the relative area of the carbonyl group compared to that of the CH_2 peak band at *ca.* 1400 cm^{-1}. Second, we measured the refractive index at the absorption wavelength of dopaminechrome, 480 nm (Figure S2e).[24]

https://doi.org/10.1021/acsnano.0c10431
ACS Nano 2021, 15, 6811−6828

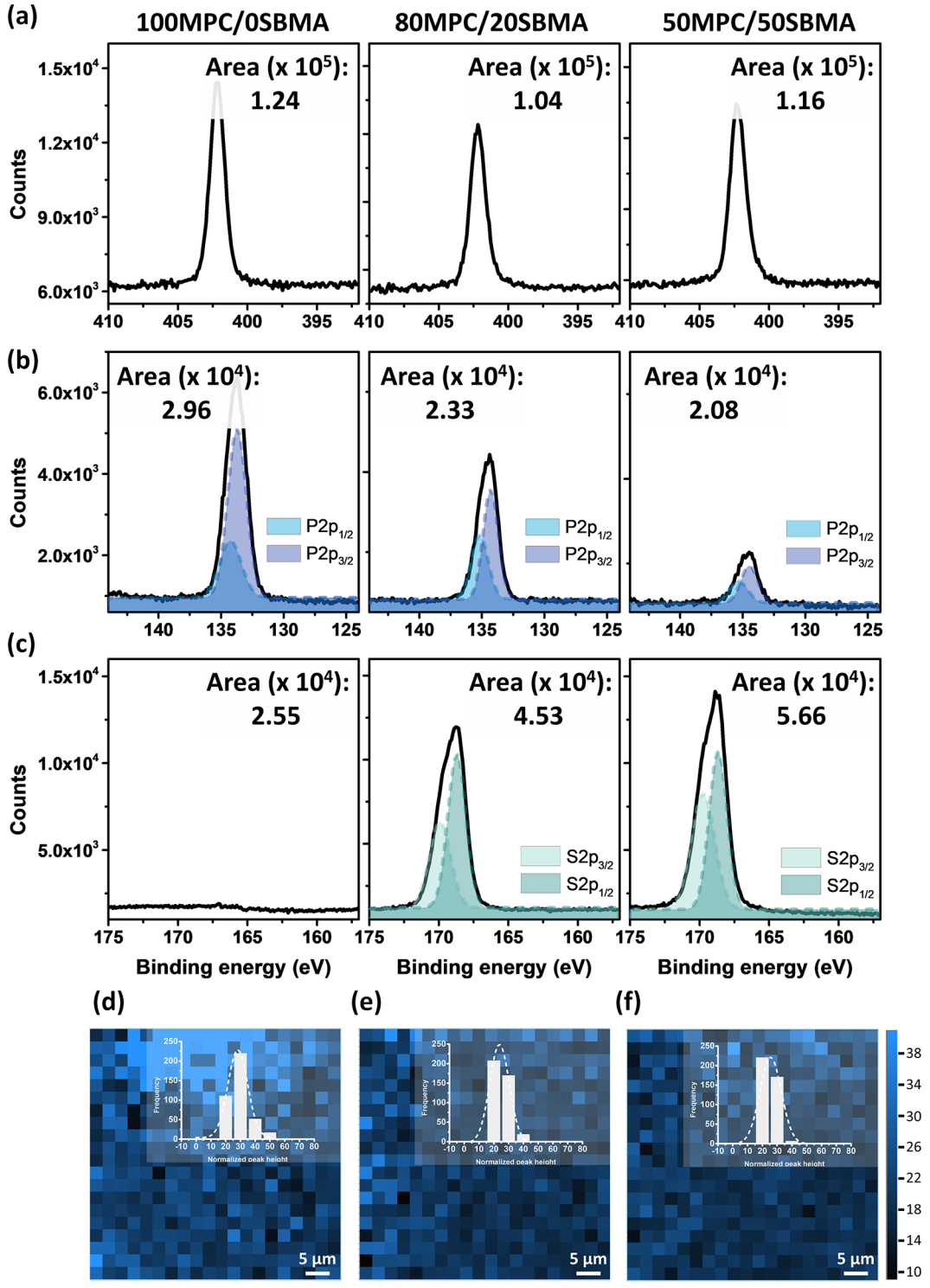

Figure 2. Design and characterization of ZPs. The XPS spectra of synthesized ZPs. (a) N 1s region, (b) P 2p region, and (c) S 2p region. The peak at 402 eV corresponds to $-R_3N^+$, 134.8 eV corresponds to $-(PO_4)^-$, and 169 eV corresponds to $-(SO_3)^-$. Color shading indicates the 2p electron spin−orbit peak splitting. (d−f) Spatial distributions of the ester group in the unit area: (d) 100MPC/0SBMA, (e) 80MPC/20SBMA, and (f) 50MPC/50SBMA. Inserted histograms highlight the uniform SI-ARGET ATRP for all ZPs. The dashed line of the histogram represents the Gaussian normal distribution.

According to the Kramers−Kronig relationship,[25] the refractive index is proportional to the absorbance. Hence, a high refractive index indicates that the undesired conformation was dominant. Analyzing both factors at once (Figure S2f), we concluded that 3 h of immobilization was optimal for maximizing the grafting density, consistent with the immobilization conditions of a previous study.[26]

Then, we designed our SI-ARGET ATRP strategy by considering the reaction kinetics shown in Figure S1b. The rate-determining step is the equilibrium between the active and dormant chains. Thus, the equilibrium constant within chain

https://doi.org/10.1021/acsnano.0c10431
ACS Nano 2021, 15, 6811−6828

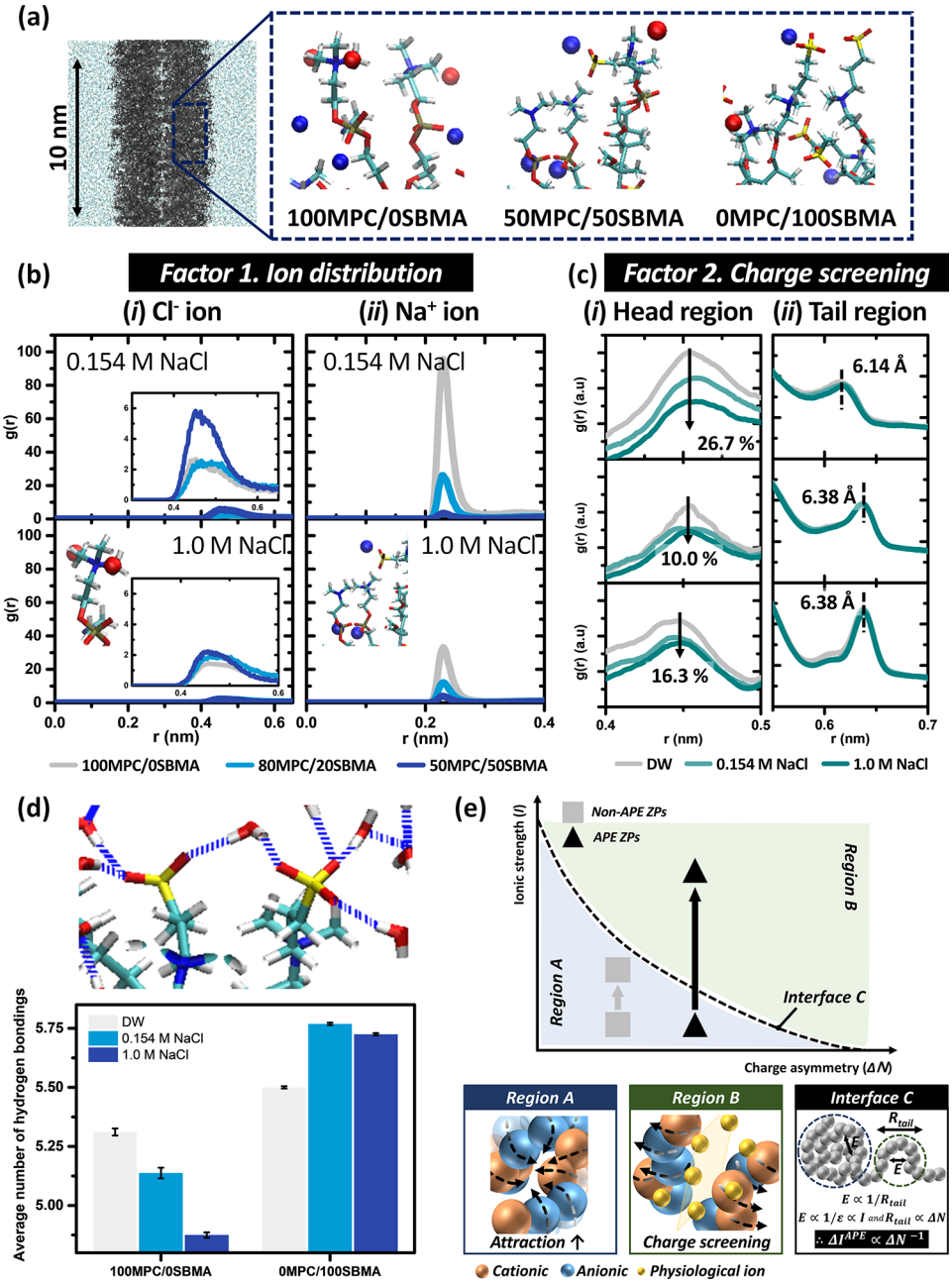

Figure 3. Investigations of APE at the molecular level. (a) Snapshots demonstrating the interactions of ions with MPC and SBMA. Carbon, oxygen, nitrogen, hydrogen, and sulfur atoms of polymers are individually represented as light blue, red, blue, white, and yellow. At the same time, Na^+ and Cl^- ions are presented as blue and red spheres. The images were created using Visual Molecular Dynamics. RDFs in terms of (b) osmotic force and (c) charge screening effect. (b) RDFs between (i) Cl^- ions and cationic moieties of the polymer and (ii) Na^+ ions and the polymer's anionic moieties. (c) RDFs between anionic moieties and cationic moieties within ZPs; from top to bottom, 100MPC/0SBMA, 50MPC/50SBMA, and 0MPC/100SBMA. (d) The average number of hydrogen bonds per zwitterionic building block as a function of salt concentration. Hydrogen bonds between water molecules and building blocks were represented as dotted blue lines. (e) Schematic demonstrating the biphasic behavior and interface of APE ZPs (black ▲) unlike non-APE ZPs (gray ■)

activation ($k_{activation}$) and deactivation ($k_{deactivation}$) regulates the polymerization rate. $CuBr_2$ is the primary catalyst and increases the equilibrium constant,[27,28] whereas 2,2′-bipyridine (bpy) enhances the solubility of $CuBr_2$ in polar solvents. Besides, we used L-ascorbic acid to reduce the oxidized copper and minimize the chain termination between active chains. Thus, using L-ascorbic acid, the "*graft from*" polymerization progressed favorably under ambient conditions without an inert gas purge. In addition, the choice of solvent significantly regulated the reaction rate between active and dormant chains. Generally, water molecules activate the propagating chains, resulting in fast growth with high chain termination, whereas methanol plays the opposite role. Therefore, a water/methanol mixture solvent with a volume ratio of 1:1 was chosen to achieve a reasonable growth rate with minimal chain termination.[29]

Characterization of Synthesized ZPs. We double-checked that the measured molecular weights were acceptable since the molecular weight is the critical factor determining the chain collapse (Figure S4). Based on the inequality

https://doi.org/10.1021/acsnano.0c10431
ACS Nano 2021, 15, 6811−6828

$|f_+ - f_-| < 1/\sqrt{N}$, where the left term is the net charge threshold for collapse, and N is the number of monomers in the polymer, the probability for chain collapse with the substrate increases as the molecular weight increases.[30] Thus, the molecular weights of the synthesized ZPs are appropriate to minimize chain collapse.

A random copolymer is essential to achieve the APE (see next section). Thus, we verified that the monomers within the synthesized ZPs were randomly distributed (Figure S5), as observed in other studies wherein random copolymers were obtained by one-pot copolymerization.

Through X-ray photoelectron spectroscopy (XPS), water contact angle (WCA), and Raman spectroscopy, we concluded that surface modification with ZPs had been successful. Because both MPC and SBMA contain $-R_3N^+$ groups, the peak area variation in the N_{1s} spectrum was negligible (Figure 2a). When the mole fraction of MPC within the random copolymer (F_1) increased, the area of the MPC-specific PO_4^- peak was enhanced (Figure 2b). Similarly, the mole fraction of SBMA (F_2) and the SO_3^- peak area showed a proportional relationship, and the maximum increase was 220% (Figure 2c). There were no significant deviations in the C_{1s} spectrum; however, there was a negative correlation between the C−O peak and F_2 (Figure S6a−c). Because MPC contains three times the number of C−O groups than SBMA, the portion of C−O groups decreased as F_2 increased. These extraordinarily sensitive results could be achieved only through XPS because it provides *ca.* 95% of the elemental composition within the first 10 nm of the surface.[31]

The surface-immobilized ZPs influence the substrate wettability, especially the hydrophilicity, because of the strong dipole pairing with water molecules.[11,13,32] When the ZPs were introduced onto the flat silicon wafer (roughness ≈0.517 nm), the substrate became superhydrophilic: WCA < 5° (Figure S6d). Thus, the water droplet spread out over the surface, forming a thin hydration layer within 5 s of touching the substrate (Supporting Movies S1−S3). We used another substrate for double-checking the improved hydrophilicity induced by the ZPs. Thanks to the adhesive catechol group, the ZPs can be attached to various substrates, including poly(methyl methacrylate) (PMMA) and glycol-modified polyethylene terephthalate (PETG) resins, which are frequently used in dental clinics. The ZPs effectively improved the hydrophilicity of both resins. Especially, the pristine PMMA resin was fairly rough (roughness ≈124.6 nm), and the hydrophobic PMMA (WCA ≈ 90°) became hydrophilic (increasing by approximately three times) after surface modification (Figure S6d).

Even when the bacteria are only attached in a limited area, they can quickly grow and form a resistant biofilm. Thus, the uniform immobilization of ZPs across all regions of the substrate is essential. We confirmed the even surface modification by using Raman spectroscopy, and the results are summarized in Figure 2d−f. In detail, we tracked the spatial distribution of the ester vibration at 1570 cm^{-1}, which is present in both MPC and SBMA. The histogram in the inset of Figure 2d−f suggested that no pixel converged to zero intensity, meaning the ZPs uniformly covered the substrate.

Parameters Necessary to Achieve the APE. APE is an extraordinary actuation of ZPs exposed to *in vivo* ionic solutions (Figure 1a). The ions screen out the inter- and intrachain attractive forces,[33] resulting in the APE (Figure 1b). However, in-depth studies of the APE are lacking. Therefore, we identified the following molecular parameters and established a theoretical basis for the APE.[19,20] As proof of our hypothesis, we investigated the molecular differences in MPC (100MPC/0SBMA) and SBMA (0MPC/100SBMA), whose responses to physiological ions are significantly different. The APE does not occur in MPC-based polymers,[17,34] but occurs in those based on SBMA.[19]

The ionic dynamics, an influential factor regulating the APE, were investigated using molecular dynamics simulation. Main group (100MPC/0SBMA, 0MPC/100SBMA) and optional group (50MPC/50SBMA) were used for the simulation to complement the experimental observations at the atomic scale (Figure 3a). As shown in Figure S7, the mass density profiles reveal that the pure bulk water density was close to the experimental value of 993 kg m^{-3} at 310 K (the errors are within 4%). Besides, a high water density of 100−500 kg m^{-3} was observed in the region of the ZPs, suggesting sufficient hydration (Figure S7a). As shown in Figure S7b, both the cations (Na^+) and anions (Cl^-) were concentrated within the ZP, implying the favorable adsorption of ions. Thus, we concluded that our set up of molecular dynamics simulation successfully reflected the realistic characteristics of the ZPs. The defining parameters regulating APE are discussed in the next sections.

Fully Charged Zwitterionic Moieties near the Isoelectric Point. The isoelectric point (IEP) is the pH at which a specific functional group is fully charged, and the net charge of a ZP becomes zero. The APE is dependent on the attraction between charged moieties; thus, we measured and confirmed the physiological (neutral) pH is the IEP of the synthesized ZPs as follows. In general, the IEP can be predicted from eqs 1 and 2.

$$R = \frac{(1 + 10^{pK_{aH} - IEP})}{(1 + 10^{IEP - pK_a})} \quad (1)$$

$$\text{when } R = 1,\ IEP = \frac{(pK_{aH} + pK_a)}{2} \quad (2)$$

where R is the ratio of cations and anions, and pK_{aH} and pK_a are the dissociation/association constants of cationic and anionic functional groups, respectively. Considering the structural property (R = 1), the IEP of ZPs was calculated using eq 2. The pK_{aH} of the weak cationic amine groups is approximately 10.5, whereas the pK_a of strong anionic groups (sulfonic or phosphonic acids) is approximately 2.0.[33] Thus, formulaically, the IEP of synthesized ZPs was estimated to be at pH 6.25. We further investigated the IEP of ZPs by measuring the surface ζ-potential in neutral media, and the results are summarized in Table S2. Because the ζ-potentials converged to zero, we concluded that synthesized ZPs are fully charged at near-neutral physiological pH.[35]

Uniform Ion Distribution Resulting from the Osmotic Driving Force. To comprehend the APE in terms of the osmotic force, radial distribution functions (RDFs) between ions and zwitterionic groups were calculated (Figure 3b). The RDFs between Cl^- ions and positively charged nitrogen show a low peak at approximately 0.45 nm (Figure 3b-i). In contrast, sharp RDF peaks were observed for Na^+ ions and anionic O^- atoms (Figure 3b-ii). Further, the partial charge in the polymer resulted in an inhomogeneous Na^+ ion distribution. In detail, the anionic partial charge of PO_4^- was −1.595, whereas that of

https://doi.org/10.1021/acsnano.0c10431
ACS Nano 2021, 15, 6811−6828

SO_3^- was −0.954. Thus, Na^+ cations can easily bind with 100MPC/0SBMA because of the stronger Coulomb force. The high affinity of Na^+ cations for MPC has been reported previously.[36] Further, we found that the uniform distribution of ions was an essential parameter determining ion-responsive behavior.

Georgiev *et al.* reported that the osmotic component is the decisive driving force of APE.[20] In Figure S8a, we assumed that the osmotic system is composed of ZP and bulk water containing ions. To achieve equilibrium, the ions move from the *W* phase to the *ZP* phase, resulting in the osmotic force. The decreased ionic concentration in the water phase (X) is given by eq 3, where k denotes the two phase equilibrium volume ratio:

$$X = \frac{C_{S,0}^{(W)}}{1+k} \tag{3}$$

Then, the volume ratio of the ZP between the initial and equilibrium state can be obtained (eq 4):

$$\frac{V_e^{(ZP)}}{V_0^{(ZP)}} = \frac{V_0^{(W)}}{V_0^{(ZP)}}\left(\frac{1+k}{k} - \frac{V_e^{(W)}}{V_0^{(W)}}\right) \tag{4}$$

When the polymers are highly diluted, the left term of eq 4 is >1.0, indicating the swelling of ZP. Thus, sufficient osmotic force is required to realize the APE. Eq 5 can be used as a metric to judge whether there is sufficient osmotic force.

$$C_{C^+,e}^{(W)} = C_{C^+,e}^{(PZ)} = C_{A^-,e}^{(W)} = C_{A^-,e}^{(PZ)} = \frac{k}{1+k}C_{S,0}^{(W)} \tag{5}$$

Therefore, the concentration of all cations and anions must be similar at osmotic equilibrium. From eq 5, we found that the distribution of ions between the ZPs must be uniform to achieve the APE. As shown in Figure S8b, 100MPC/0SBMA, which is not capable of APE,[17] shows tremendous RDF variations, regardless of the medium. In contrast, the ion RDFs of 0MPC/100SBMA converged to a similar level, indicating the possibility of APE. These results allow us to establish a theoretical basis to predict the occurrence of the APE: If a highly negative moiety is introduced, there is no osmotic driving force, and the APE cannot occur.

Charge Screening Effect between ZPs with Significant Charge Asymmetry. The osmotic driving force does not include the effect of the inter- and intrapolymer interaction energy on the APE. Conceptually, ions reduce the attractive interactions within APE ZPs *via* charge screening effect.[13] Thus, we investigated the attractive energy (E) in terms of the RDFs between anionic O atoms and cationic N atoms (Figure 3c). We obtained two significant results that reflect the charge screening effect: the significant influence of (i) the material properties in the tail region and (ii) the property of the environment in the head region. Subsequently, the profound correlation between the APE and charge screening effects was investigated.

First, we interpreted the effects of building blocks from the chain length (the tail region in Figure S8c–e). Herein, we treated a single fully charged ZP chain into two parts: the chain head having strong internal interactions and the tail having relatively weak interactions. Then, we ordered the tail length (R_{tail}) in terms of charge asymmetry (ΔN), assuming a similar scaling theory to that of polyampholytes.[30,37] Herein, ΔN is the difference in charge density (e nm^{-3}) between cationic and anionic functional groups. The size of the electrostatic tail (ξ_{tail}) can be deduced from eq 6:

$$\xi_{tail} \approx b(uf^2)^{-1/3} \tag{6}$$

where f is the mole fraction of charged monomers, and u is the ratio of the Bjerrum length to the Kuhn length (b). From eq 6, the relationship between R_{tail} and ΔN can be derived using eq 7:

$$\text{From eq 6; } R_{tail} \approx \frac{\xi_{tail}\Delta N}{g_{tail}} \approx b\Delta N(uf^2)^{1/3} \tag{7}$$

$$\text{From eq 7, } R_{tail} \propto \Delta N \tag{8}$$

where g_{tail} is the number of monomers in the tail. It is reasonable to consider f as 1.0 (Figure S5) and the temperature-dependent terms, u (7.14 Å at room temperature)[30] and b, as constant values. As shown by eq 8, R_{tail} is proportional to ΔN.

Figure 3c-ii shows that RDF peak intensities in the tail region and R_{tail} were increased by *ca.* 130% for 0MPC/100SBMA with respect to 100MPC/0SBMA (Table S3). Eq 8 represents the conformational change induced by ΔN because the ΔN value of SBMA (*ca.* 1.5 e nm^{-3}) is greater than that of MPC (*ca.* 0.0 e nm^{-3}).[15] Herein, note that ΔN is the critical material properties of the polymer building block.

Second, we interpreted the head region in terms of the charge screening effect (the head region in Figure S8c–e). In detail, we modeled charge screening using the attractive energy between zwitterionic moieties (E_{ZP})[30] (eq 9):

$$E_{ZP} = \sum_{i-1}^{N} v_i e V_p(z_i) + \sum_{i<j}^{N-1}\frac{K}{2}(|r_i - r_j|^2) + \sum_{i<j}^{N}\frac{v_i v_j e^2}{4\pi\epsilon_0|r_i - r_j|} + \sum_{i<j}^{N} u_{ij}^{hc}(r_{ij}) \tag{9}$$

$$\text{Thus, } E_{ZP} \approx \sum_{i-1}^{N} v_i e V_p(z_i) + \text{constant} \tag{10}$$

$$\text{From eq 10; } E_{ZP} \propto \frac{1}{I} \tag{11}$$

where v is the valence, e is the electron charge, and N is the number of monomers. The second term of eq 9 is constant because the spring constant (K) is 13.6 × 10^{-3} N m^{-1}. In addition, the third term is zero because the local charge correlation ($h_{corr} = \sum v_i v_j/N - 2$) of the random polymer is zero. In the same manner, the fourth term is also zero. Thus, we obtained the eq 10.

From eq 10, the effective potential between polymers and ions ($V_p(z_i)$) is the main parameter determining E_{ZP}. Because the ions reduce the dielectric permeability, the ionic strength (I) of the media is inversely proportional to $V_p(z_i)$.[38] Therefore, E_{ZP} is weakened in high ionic strength media, which represents the charge screening effect (eq 11). Technically, E_{ZP} mainly affects the spatial properties of the head group.

Figure 3c-i shows that the RDF within the head region is reduced for all ZPs as I increases. Considering I for each media, the probability of the head region decreased as the E_{ZP} was reduced. Thus, eq 11 represents the charge screening induced by the surrounding ions.

However, eqs 8 and 11 represent the effects of the materials and surrounding media on the APE. Thus, we merged both

https://doi.org/10.1021/acsnano.0c10431
ACS Nano 2021, 15, 6811–6828

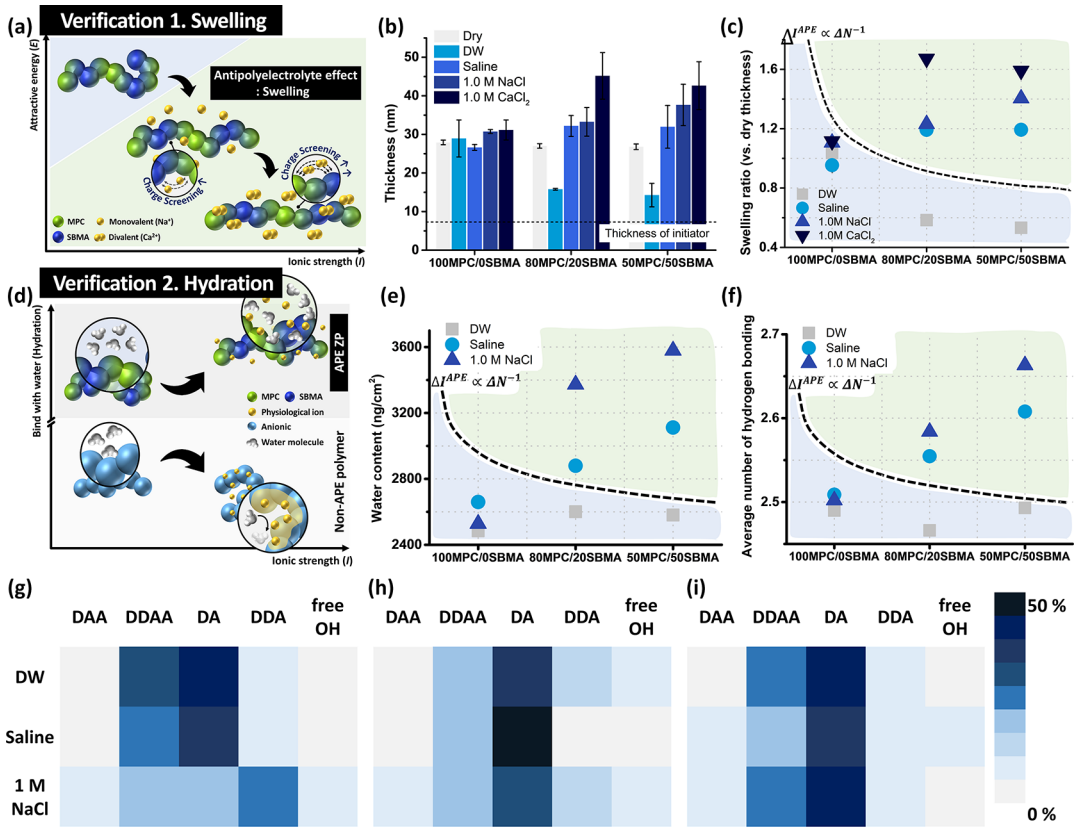

Figure 4. Verifications of APE with respect to (a–c) swelling and (d–i) hydration dynamics. (a) Swelling dynamics of APE ZPs in the presence of various cations. The (b) thickness and (c) swelling ratio of ZPs under different media. (d) Contrasting hydration dynamics in (top) APE ZP and (bottom) a general polyelectrolyte. (e) Water content within ZPs. The color shadings and dashed lines in (a, c, e, f) correspond to the biphasic behavior of APE ZPs in Figure 3e. (f) The average number of hydrogen bonds. Heat maps of five types of hydrogen bond in (g) 100MPC/0SBMA, (h) 80MPC/20SBMA, and (i) 50MPC/50SBMA.

equations considering the inverse relationship between R_{tail} and E_{ZP} (eq 12).

$$\text{From eqs 8 and 11, } \Delta I^{APE} \propto \Delta N^{-1} \tag{12}$$

where ΔI^{APE} indicates the threshold elevation in ionic strength at which the charge screening begins to dominate. We tested eq 12 in terms of the hydration. The number of hydrogen bonds should increase at the APE threshold, that is, where E_{ZP} decreases. As shown in Figure 3d, 0MPC/100SBMA, which has a higher ΔN, showed increased hydration in the simulated range. A smaller ΔI^{APE} meant that fewer ions effectively screen out the attractive interactions of the ZPs. We concluded that as the charge screening becomes considerable, the probability of APE would increase.

Biphasic Model to Verify the APE. We developed a biphasic model to summarize the ion-responsive behavior of APE ZPs exhibiting APE (Figure 3e). The biphasic model comprises two regions, depending on the ionic strength and charge asymmetry. In the low-ionic-strength environment, the attractive interactions within non-APE or APE ZPs (E_{ZP}) dominate because of negligible charge screening (blue shading in Figure 3e). For the same increase in ionic strength, E_{ZP} of APE ZPs is significantly reduced by the effective charge screening (green shading in Figure 3e). However, general ZPs with negligible charge asymmetry hardly move to the green shading region, indicating that they do not exhibit the APE. Further, the interface between two regions (dashed line in Figure 3e) can be thermodynamically determined using eq 12. We also applied the biphasic model experimentally, as discussed in the next section.

In summary, we have established a theoretical basis for the APE. For APE ZPs, the following factors must be considered: (i) moderately partially charged functional groups enable the uniform distribution of ions by osmotic forces, and (ii) a large ΔN causes a charge screening effect in ionic solutions.

Figure 3 shows that 0MPC/100SBMA was best from the viewpoint of APE. However, a gel-like structure, unsuitable for surface modification, was formed (Figure S9), and the structure was confirmed by applying the shear stress (Supporting Movies S4–S5). Thus, we excluded 0MPC/100SBMA from the experimental group.

Verification of the APE. Because APE is a consequence of the E_{ZP} reduction on significant charge screening, the following changes in APE ZPs occur under biological conditions; (i) increased thickness[20] and (ii) enhanced hydration.[11] Regarding both as intuitive indicators of APE, we conducted experimental verification to determine whether the synthesized ZPs are genuinely exhibiting APE, including (i) determining the swelling ratio (Figure 4a–c) and (ii) visualizing hydration dynamics (Figure 4d–i). We conducted the experiments in an ionic solution containing a single salt (one type of cation and anion), and the concentration was varied within the physiological range.

Comprehension of the Swelling Behaviors. We measured the thickness of surface-immobilized ZPs using the ellipsometer (Figure 4b). Since the polymer volume fractions

https://doi.org/10.1021/acsnano.0c10431
ACS Nano 2021, 15, 6811–6828

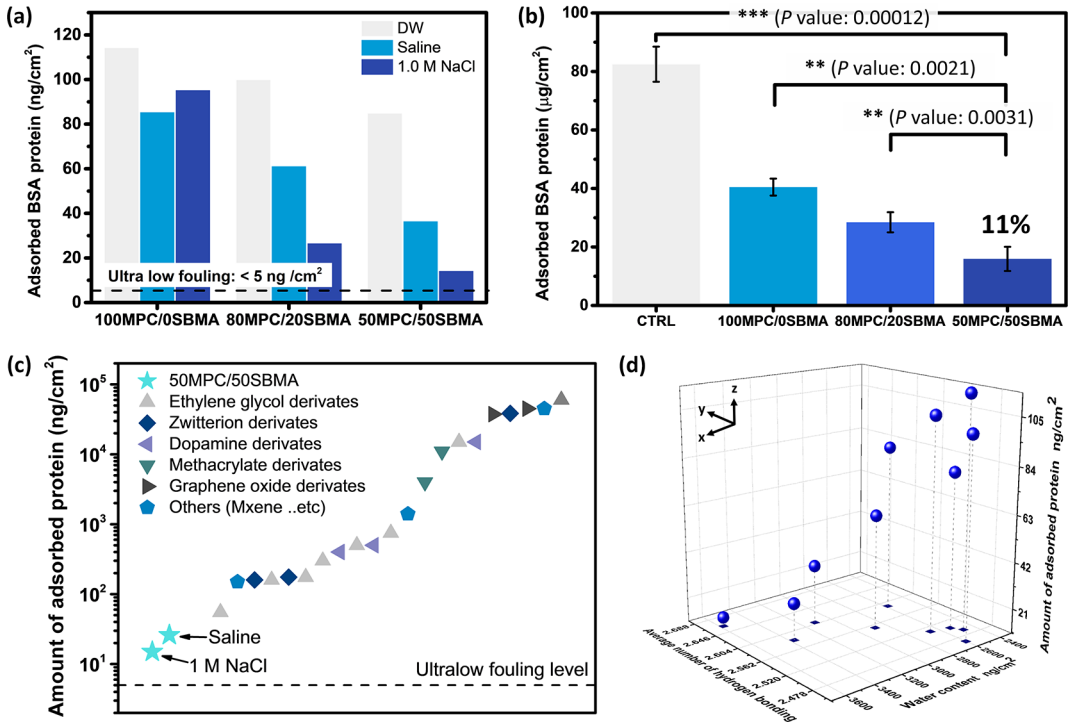

Figure 5. ***In vitro*** **antifouling assay with the model protein, BSA. The biofouling time increased from (a) 20 min to (b) 6 h. The different assay tool was adapted; (a)** ***in situ*** **QCM and (b) micro-BCA assay. In Figure 5a, the dashed line emphasizes the ultralow fouling level. Here, the flat silicon wafer was adapted as the substrate (*i.e*, positive control, CTRL). (c) Comparison of the antifouling property of 50MPC/50SBMA with various materials. Light green (★) indicates the 50MPC/50SBMA exhibiting APE under the ionic solutions. Light gray (▲), navy (◆), light purple (◀), green (▼), and dark gray (▶) symbols indicate ethylene glycol, zwitterion, dopamine, methacrylate, and graphene oxide derivatives, respectively. Blue (⬟) symbol corresponds to the extra materials (*e.g.*, MXenes). The relevant references are listed in the Supporting Information. (d) Summarized result of (a) showing the proportional relationship between antipolyelectrolyte effect and antifouling property.**

of ZPs were over 40% regardless of media, the ellipsometer was an appropriate tool to measure the hydrated thickness (Figure S10).[29] On the addition of sodium chloride, E_{ZP} decreased for 80MPC/20SBMA and 50MPC/50SBMA because of their large ΔN values (Figure 4a).[39] As shown in Figure 4c, both ZPs energetically swelled in the monovalent solutions. When dealing with all polymers, we deduced the apparent biphasic behavior (background of Figure 4c) based on our theory: (i) The APE occurs only in ZPs with large ΔN, and (ii) a high ionic strength induces a more substantial APE.

In addition, we used the 1.0 M $CaCl_2$ solution to study the APE further, predicting that 80MPC/20SBMA and 50MPC/50SBMA might swell more in the presence of $CaCl_2$. As previous studies have suggested, we found that the zwitterion-cation association was more significant than the zwitterion-anion association (Figure 3b).[39−41] Besides, the kosmotropic cations preferentially associate with anionic moieties with a higher partial charge and *vice versa*.[32,40] Thus, divalent Ca^{2+} would have a stronger affinity for SO_3^- and result in significant charge screening. Moreover, based on eq 11, we believe that 1.0 M $CaCl_2$ would significantly reduce the attractive energy (E_{ZP}) because of the high ionic strength. The experimental results in Figure 4c confirmed our prediction, suggesting that 80MPC/20SBMA and 50MPC/50SBMA are able to APE.

Visualization of the Hydration Dynamics. Figure 4d shows the hydration behavior of APE ZP and that of a general polyelectrolyte. Theoretically, the dipole−dipole interactions with water (hydration) become stronger as E_{ZP} is weaker.[11] To confirm the theoretical relationship, we visualized the hydration dynamics concerning (i) the mass of water (Figure 4e) and (ii) the number of hydrogen bonds (Figure 4f).

We measured the bulk water mass within the ZP brushes, denoted as the water content (Figure S11a). Thanks to the overwhelming hydration ability of ZPs, their overall water contents are higher than those of other antifouling polymers (Figure 4e), that is, four times higher than poly(*N*-isopropylacrylamide).[42] Because the overall trend of water contents shown in Figure 4e is biphasic, we concluded that 80MPC/20SBMA and 50MPC/50SBMA have the APE capability.

Second, we performed Raman spectroscopy to investigate the average number of hydrogen bonds per water molecule (N_{HB}).[43] In our previous study, we found that Raman spectroscopy is an appropriate method to interpret the local hydrogen dynamics of water molecules (Figure S11b,c).[44] Five types of hydrogen bonds, namely DAA, DDAA, DA, DDA, and free-OH (where D is a donor and A is an acceptor; Figure S11b), were detected in the Raman spectrum from 3000 to 4000 cm^{-1} (Figure S11c). We determined N_{HB} using eq 13:

$$N_{HB} = 4R_{DDAA} + 3R_{DDA} + 3R_{DAA} + 2R_{DA} \quad (13)$$

where R_{DDAA}, R_{DDA}, R_{DAA}, and R_{DA} denote the area ratios of the bands corresponding to DDAA, DDA, DAA, and DA, respectively. The area ratios are summarized in heat maps in Figure 4g−i. DA was the most significant interaction under all conditions because the dipole−dipole interaction is he primary driving force for hydration. Further, the difference between all hydrogen bonds, except free-OH, became small as ionic

https://doi.org/10.1021/acsnano.0c10431
ACS Nano 2021, 15, 6811−6828

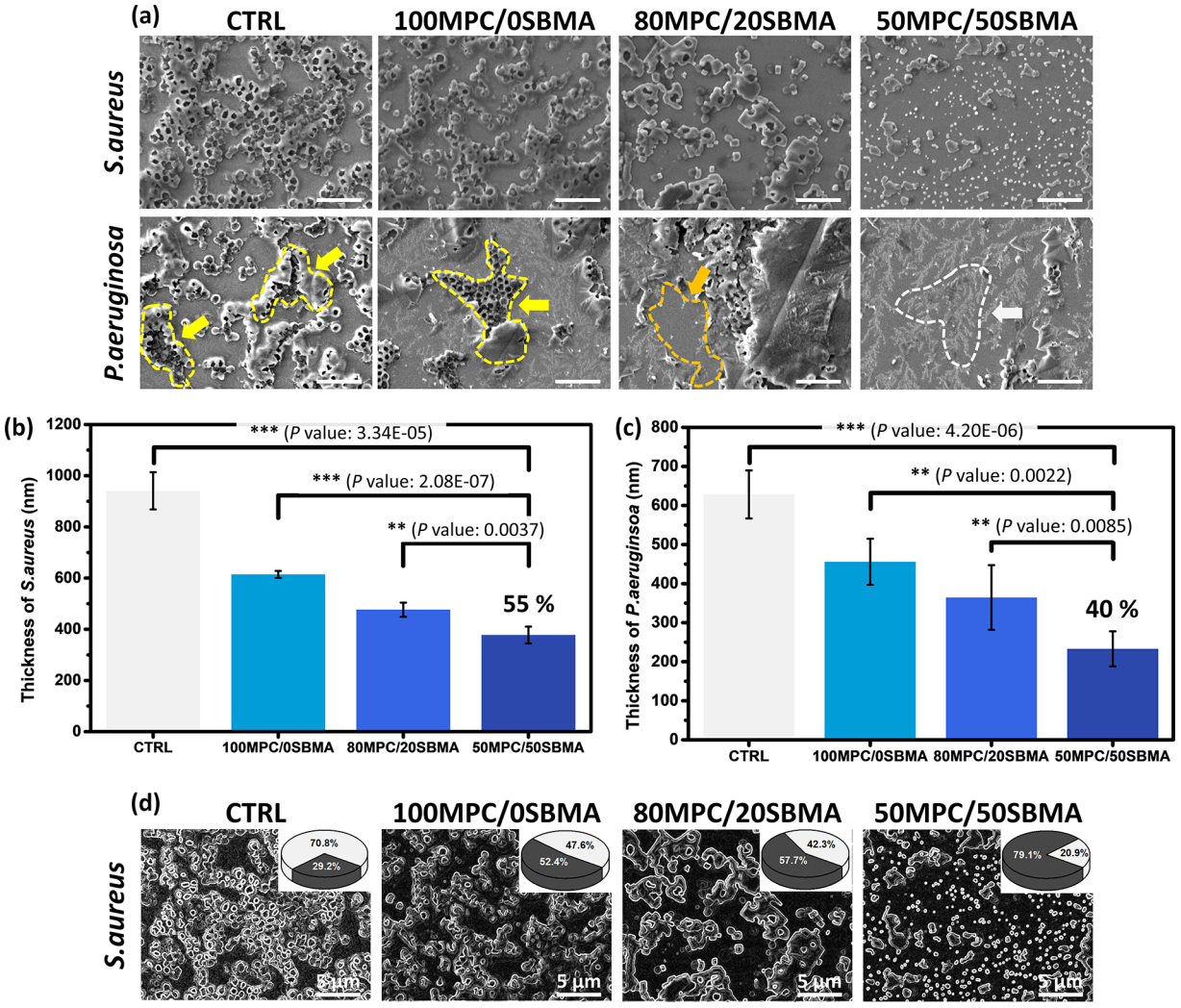

Figure 6. *In vitro* **antifouling assay with the single bacterial model;** ***S. aureus*** **and** ***P. aeruginosa*****.** (a) SEM image of model bacteria over the samples. The scale bar indicates 5 μm. The yellow, orange, and white arrows individually indicate the multilayered bacteria, pristine substrate, and ZP. The thickness of multilayered bacteria biofilm: (b) *S. aureus* and (c) *P. aeruginosa*. (d) The color contrast of SEM image of *S. aureus*. The commercial ImageJ software was adopted. White lines indicate the boundaries between bacteria and substrate. In the inserted pie chart, light gray and dark gray represent the area percentage of the bacteria and pristine substrate, respectively. The flat silicon wafer was adopted as the substrate.

strength increased. Thus, the variations in N_{HB} (Figure 4f) show the same biphasic trend as the swelling ratio and water content, which the APE regulates. In more detail, the more significant proportion of SBMA increased ΔN, resulting in more considerable swelling and hydration by APE.

Thus, we concluded that 100MPC/0SBMA was non-APE ZP; otherwise, 80MPC/20SBMA and 50MPC/50SBMA were the APE ZPs. In detail, 50MPC/50SBMA represented the most significant APE due to its considerable osmotic force and charge screening effect (Figure 3). Especially, 50MPC/50SBMA has the optimal composition in terms of the APE and possibly exhibits superior antifouling performance, as discussed in the next section.

Enhanced Antifouling Performance under Progressively Harsh Conditions. The antifouling effect of the ZPs is modulated by hydration, which results in an energy barrier preventing the initial fouling by biopollutants.[10] Therefore, note that ZPs are effective in reducing the initial planktonic fouling. Notably, APE maximizes the already superior hydration of APE ZPs in ionic solutions (Figure 4e,f). Because the human body has ionic solutions (*i.e.*, water containing the ions, proteins), we expected to observe impressive *in vivo* antifouling performance of the APE ZPs.

Most previous studies concerning antifouling polymers have investigated only moderate protein adsorption using QCM-D. Thus, we developed a series of procedures to mimic progressively more stringent *in vivo* conditions, from *in vitro* protein adsorption to *in vivo* biofouling (Figure S12).

Moderate Conditions: *In Vitro* Adsorption of a Single Protein Model. The two protein tools used in this study to determine protein adsorption, *in situ* quartz crystal microbalance (QCM) and bicinchoninic acid assay, have specific pros and cons. The resolution is relatively better in *in situ* QCM, approximately 1.0 ng cm^{-2}, when using 5 MHz oscillation. However, the desired measurement time of *in situ* QCM is *ca.* 20 min, which is not representative of biofouling conditions. Thus, we also used the biological, bicinchoninic acid assay, in which bovine serum albumin (BSA) adsorption is carried out for 6 h in a cell incubator. Through this complementary process, we interpreted the different protein

https://doi.org/10.1021/acsnano.0c10431
ACS Nano 2021, 15, 6811−6828

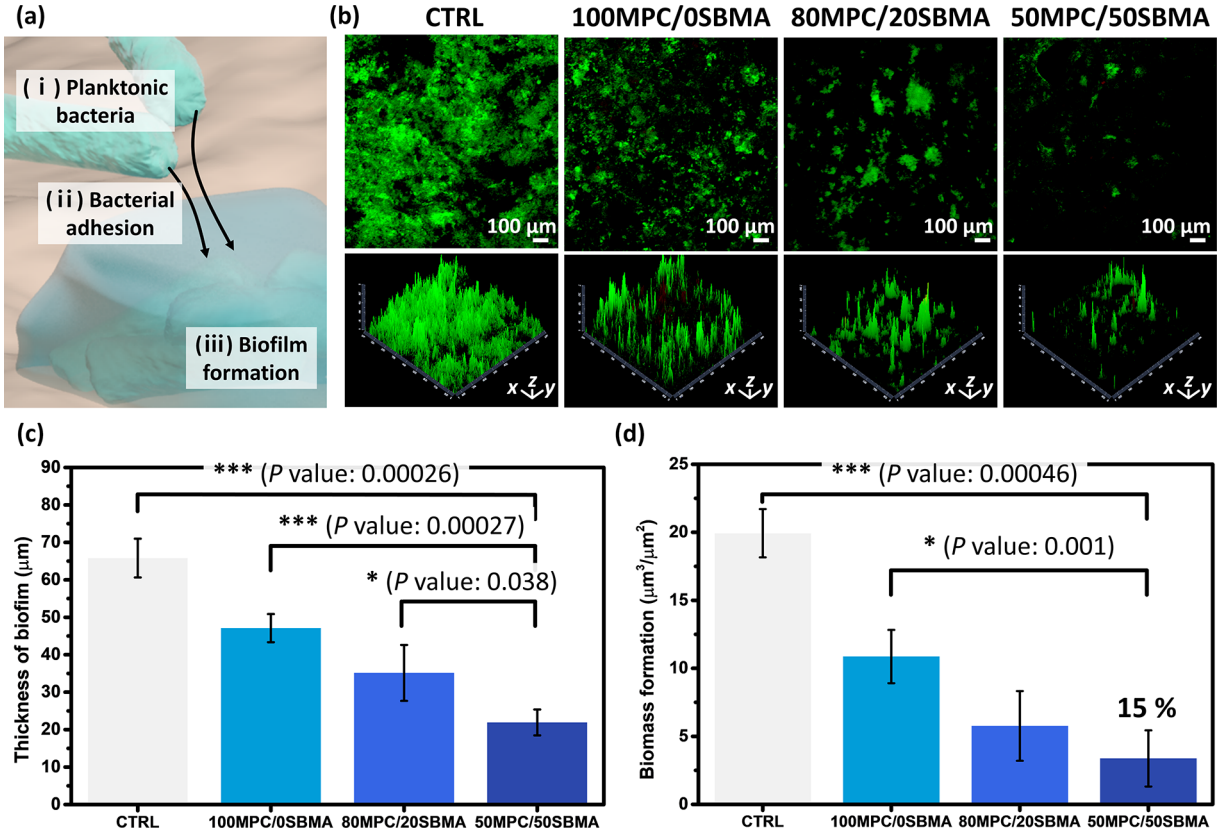

Figure 7. ***Ex vivo*** **antifouling assay with the multiple microorganism model from the human saliva; biofilm formation. (a) Schematic illustration of the bacterial biofilm formation process. (b) Confocal image of the biofilm formed over the sample. The side view image scale is 100 μm (x, y-axes) and 20 μm (z-axis). CTRL indicates PMMA resin, which the ZPs were attached. From the confocal image, (c) thickness of biofilm and (d) biomass formation were evaluated.**

adsorption dynamics in general ZP (100MPC/0SBMA) and APE ZPs (80MPC/20SBMA and 50MPC/50SBMA). We identified the protein adsorption dynamics in general and APE ZPs in detail (Figure 5a,b). The model protein, BSA, is well-known for its favorable nonspecific adsorption. The adsorbed BSA is a nutrient and can promote the attachment of bacteria *via* chemotaxis.

Because of the considerable hydration ability of MPC,[44] the antifouling performance of 100MPC/0SBMA was excellent (Figure 5a). However, the antifouling performance of 100MPC/0SBMA, unable to APE, was independent of the surrounding media. In contrast, BSA adsorption on APE ZPs was significantly reduced in the ionic solutions. Notably, 50MPC/50SBMA showed an impressive antifouling performance, only adsorbing 13 ng cm^{-2} BSA, that is, ultralow fouling level.[45] Figure 5c shows an interdisciplinary comparison of the antifouling performances. Both PEG and zwitterion derivatives showed the outstanding antifouling effects. However, none showed a similar ultralow fouling performance under physiological conditions. Thus, 50MPC/50SBMA inhibited protein adsorption to the greatest extent.

The interrelationship between three variables (APE, hydration, and antifouling ability) is shown in Figure 5d. Due to APE, the water content (x-axis) and N_{HB} (y-axis) increased simultaneously, and the antifouling performance (z-axis) was maximized. Besides, after 6 h biofouling, 50MPC/50SBMA exhibited *ca.* 89% inhibition compared to the pristine substrate (Figure 5b). Note that 50MPC/50SBMA exhibited the APE because it was in BSA solution diluted with the ionic solution, 1× PBS.

Harsh Conditions: *In Vitro* Adhesion of Single Bacterial Model. We then investigated the adhesion of a single bacterial strain during long-term incubation (Figure 6). For these experiments, we used Gram-positive *Staphylococcus aureus* and Gram-negative *Pseudomonas aeruginosa*. Even after the severe 48 h adhesion of high initial optical density, multiple layers of bacteria (yellow arrow in Figure 6a) were formed only where planktonic bacteria had been attached. In addition, the pristine substrate (orange arrow) and ZPs (white arrow) can be seen in the SEM images. Owing to the considerable hydration of 50MPC/50SBMA in the culture medium, excellent antifouling performance (regarding the biofilm thickness) was obtained (Figure 6b,c).

Because the bacterial strains have different growth dynamics, we conducted further investigations considering all axes, that is, thickness (z-axis) and bacterial coverage (x, y-axis). *S. aureus* requires passive interaction with host cells to express effector proteins (type-VII secretion system).[46] Thus, antifouling by the inhibition of planktonic *S. aureus* attachment is entirely possible. In contrast, *P. aeruginosa* actively injects effector proteins into the host cell (type-III secretion system) and easily forms multilayered structures.[47] Besides, *P. aeruginosa* produces highly sticky extracellular alginate. Therefore, the antibacterial function against *P. aeruginosa* typically depends on the prevention of initial adhesion and bactericidal treatment. The effects of different secretion systems are clearly shown in Figure 6a; *P. aeruginosa* covers the entire surface, but *S. aureus*

https://doi.org/10.1021/acsnano.0c10431
ACS Nano 2021, 15, 6811−6828

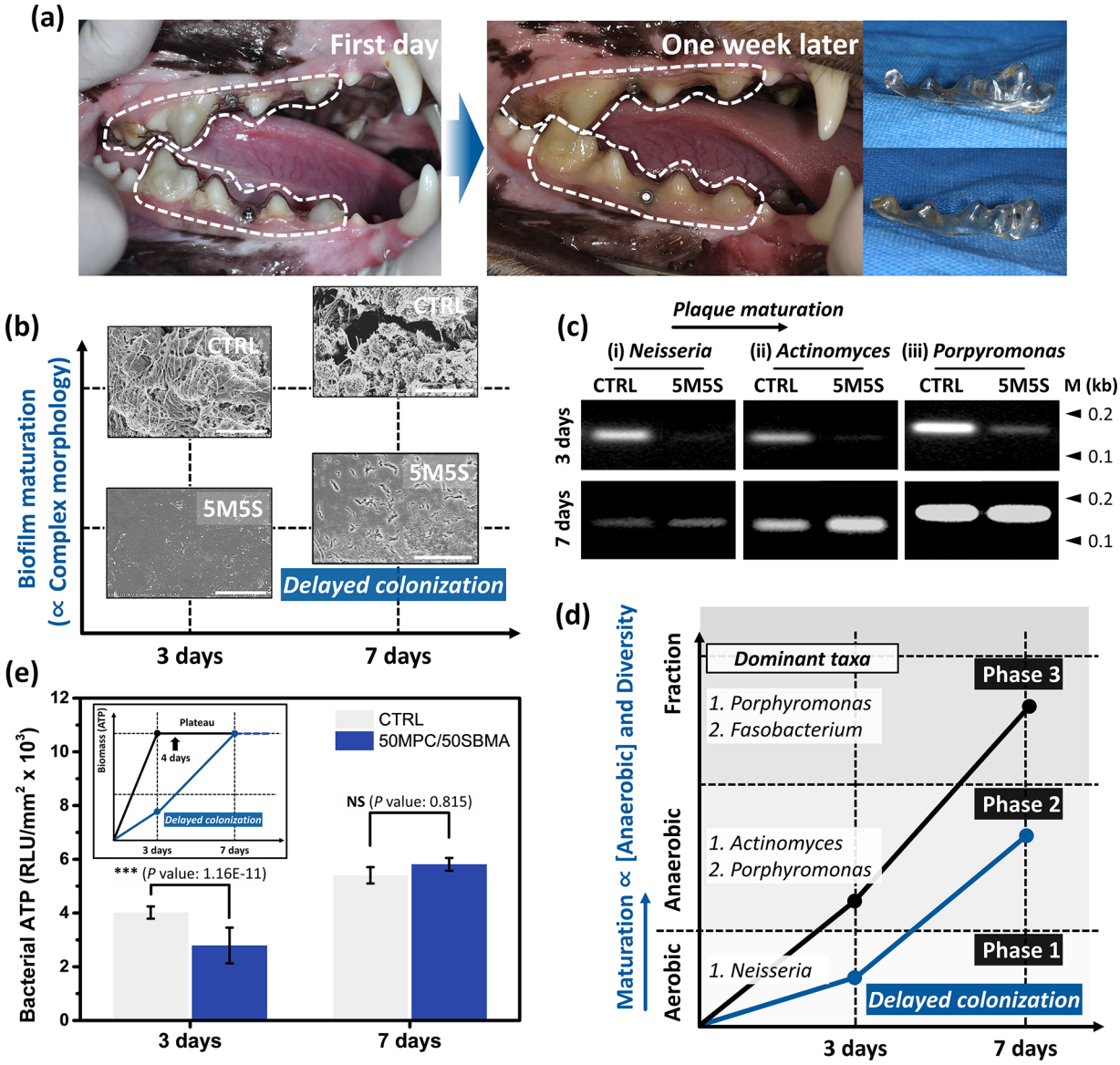

Figure 8. *In vivo* antifouling assay of canine oral bacterial biofilm. Here, PETG retainer was the positive control (CTRL), and 50MPC/50SBMA (5M5S) was the experimental group. (a) Photographs of oral biofouling assay using a medium-sized dog model. (b) Maturation of canine oral biofilms evaluated *via* SEM. Representative images are shown as insets in the maturation trend curve. The scale bars in SEM images indicate 20 μm. Figure S14 shows SEM images of inner and outer surfaces. Effects of 50MPC/50SBMA (5M5S) on the composition and viability of dental plaque biofilms were further investigated. (c) Comparisons of bacterial genomic DNA derived from the members of *Neisseria*, *Actinomyces*, and *Porphyromonas*. *M* denotes the molecular weight of the marker. (d) Suggested variation in biofilm composition with maturation. The scattered line graph was reorganized from (c). (e) Viability of the bacterial cells in the dental plaque biofilms determined by ATP-based luminescence. RLU denotes the relative light units. In the inset curves, black and blue correspond to CTRL and 50MPC/50SBMA, respectively.

is present in separated regions. Thus, we carried out the spatial analysis of *S. aureus* (Figure 6d). As summarized in the inset pie charts, the biofilm area portion was significantly reduced from 71% (CTRL) to 21% (50MPC/50SBMA). Therefore, we confirmed the considerable antifouling performance of APE ZP using the single bacterial models.

Harsh Conditions: *Ex Vivo* Biofilm Formation with a Multiple Microorganism Model. The solvated 50MPC/50SBMA could overcome the attached bacteria's gravitational force *via* the APE (Figure S13). Thus, we conducted a further antifouling assay, *ex vivo* biofilm formation (Figure 7). Our *ex vivo* biofilm formation model is a realistic model of harsh dental treatments such as orthodontic processes because of the (i) favorable attachment of multiple microorganisms from donor saliva, (ii) use of PMMA as a substrate, which is widely used in dentistry, and (iii) long-term incubation period (48 h). During *ex vivo* experiments, we used saliva from donors who had not taken antibiotics for a specified period. Saliva typically contains several bacterial species, including *Streptococcus oralis*, *Actinomyces naeslundii*, and *Veillonella parvula*. These organisms form the resistive biofilms because of favorable cell−cell interactions (Figure 7a). Using adhesive catecholamine, we performed SI-ARGET ATRP on PETG, which, as mentioned, is one of the most common materials in dentistry, for example, in clear overlays.[48] Because the PETG surface is rougher than the silicon wafer substrate used in *in vitro* experiments,

https://doi.org/10.1021/acsnano.0c10431
ACS Nano 2021, 15, 6811−6828

bacterial adhesion onto PETG should be greater than that on silicon.[49] In addition, the grafting density of the hydrophilic zwitterionic monomers must be low because PETG (WCA ≈ 85°) is more hydrophobic than silicon wafer (WCA ≈ 50°). Thus, our *ex vivo* biofilm formation model is a realistic model of the harsh dental environment. Even in a harsh biofouling environment, 50MPC/50SBMA effectively inhibited initial bacterial adhesion. In particular, the area without biofilm was more extensive than that for the 100MPC/0SBMA (black region in Figure 7b). Further, the thickness of the biofilm over 50MPC/50SBMA was signifiantly reduced (*ca.* 65%) compared to that on pristine PETG (Figure 7c).

Biofilm-forming microorganisms express resistance to both innate/adaptive immune systems and antibiotics. Thus, it is challenging to eliminate biofilms, such as the thick green regions in Figure 7a, once formed. We quantitatively measured the resistance to the biofilm using the *z*-axis (thickness) and *x*, *y*-axes (biofilm coverage), denoted as biofilm formation ($\mu m^3/\mu m^2$). Thus, we concluded that 50MPC/50SBMA inhibited biofilm formation by approximately 85% compared to pristine PETG (Figure 7d).

Harshest Conditions: *In Vivo* Oral Biofouling in a Medium-Sized Dog Model. If the antifouling effect of 50MPC/50SBMA is maintained in the *in vivo* oral environment, APE ZP has the potential to be applied in other *in vivo* applications. Therefore, we conducted *in vivo* oral biofouling assays using a medium-sized dog model (Figure 8a), a beagle without oral hygiene management ability. Concerning medical implants, the *in vivo* oral environment is the dynamic condition, showing (i) changes in physiological conditions (*e.g.*, acidity, moisture, temperature), (ii) reactions to the external environment, and (iii) continuous macroscopic mechanical stress induced by mandibular movement during mastication and occlusion. Further, an implantable oral medical device must be worn all day long. Thus, it was questioned whether the nanoscale polymer is still useful *in vivo*. To the best of our knowledge, this is the leading study to use a medium-sized animal to test antifouling polymers in medical devices during intraoral use. 50MPC/50SBMA was chosen because of its active APE and significant antifouling performance.

Biofilm life cycle comprises (i) reversible/irreversible attachment of planktonic bacteria, (ii) biofilm maturation, and (iii) dispersion of subpopulations along with biofilm erosion.[50] In particular, biofilm maturation is the state when biofilm structure with maximum thickness formed the channels to facilitate the nutrient diffusion.[50,51] Quantitative indexes of biofilm maturation could be (i) the formation of complex morphology, (ii) the change of inner environment from aerobic to anaerobic, and (iii) the increased diversity of bacterial strains. In this study, Figure 8b supports the discussion of the morphological issue, and Figure 8c,d was conducted to evaluate the environmental and populational issue. In addition, the dental plaque is a microbial biofilm ecosystem containing hundreds of species.[52]

First, we evaluated the maturation of biofilms based on their morphologies (Figure 8b). Only a few bacteria adhered to 50MPC/50SBMA, and they showed a less mature, simpler biofilm morphology. The individual variations in canine oral microbiota were attributed to the biofilms' morphologies in each beagle test dog. As shown in Figure S14a, multiple layered, complex biofilms were observed on the outer and inner surfaces of the CTRL on day 3, indicating a matured biofilm. Herein, the terms "inner" and "outer" indicate the surface adjacent to the teeth and exposed to the oral cavity, respectively. Unlike the outer surfaces of the CTRL sample, few bacteria adhered to the outer surfaces of 50MPC/50SBMA, and the biofilm had a less mature morphology (Figure S14b). In addition, biofilm formation was also suppressed on the inner surfaces of 50MPC/50SBMA, and a much simpler biofilm was formed (dog ID 1), or clean areas without bacteria were noticeable (dog ID 2−3). Interestingly, among 50MPC/50SBMA surfaces, fewer bacteria adhered to the outer surfaces than the inner surfaces. This difference is probably due to self-cleaning effects, such as saliva, tongue, and mucosal movements, which significantly affect the outer surfaces. On day 7, the amount of biofilm on 50MPC/50SBMA was greater than on day 3. However, the biofilm structures were simpler and less mature on 50MPC/50SBMA than those of the CTRL (Figure S14c,d).

Second, we evaluated the biofilm (*i.e.*, dental plaque) maturation in terms of inner environment and populations. In detail, we interpreted the *in vivo* antifouling mechanism based on the relative amounts of specific DNA sequences exploiting the polymerase chain reaction (PCR) (Figure 8c). Dental plaque formation begins by the initial colonizers' adhesion to the salivary pellicle surface. Then, later colonizers attach to the initial colonizers. As the dental plaque matures, environmental conditions (such as pH and nutrients) alter, leading to significant shifts in microbial populations: (i) Major colonizers change from initial/aerobic strand to later/anaerobic strand, and (ii) the absolute diversity of bacterial strands increases. Takeshita *et al.* also reported that the species diversity particularly elevated between days 5 and 7 (Figure 8d).[53]

To analyze the bacterial community compositions of the dental plaque, we selected three representative bacterial genera and their specific primer: *Neisseria*, *Actinomyces*, and *Porphyromonas* (Table S4). Herein, *Neisseria* represents an initial colonizer, and *Actinomyces* and *Porphyromonas* are representative later colonizers.[54] On day 3 (first row in Figure 8c), the dental plaque on CTRL contained significantly more bacteria than 50MPC/50SBMA. Interestingly, *Porphyromonas* was particularly prominent. This result indicates that the dental plaque formation on CTRL was favorable. The plaque on CTRL reached phase 2 on day 3 (Figure 8d), and CTRL contained a relatively large population of facultative anaerobic bacteria. It has been reported that *Neisseria* are abundant in the initial stage of biofilm formation (phase 1, Figure 8d), and their relative proportion decreases as the plaque matures.[54] Thus, the relative proportion of *Neisseria* on CTRL (see Figure 8c-i) was less on day 7 than in the initial stages, which is proof of reaching phase 3 (Figure 8d).

In contrast, for 50MPC/50SBMA, the three PCR bands showed weak signals on day 3. In detail, the intensities were reduced by *ca.* 81.2% (*Neisseria*), 88.1% (*Actinomyces*), and 71.0% (*Porphyromonas*) compared with those of CTRL. These results strongly suggest that 50MPC/50SBMA reduced bacterial adhesion and delayed plaque formation. However, all signals increased on day 7 (second row in Figure 8c). In particular, the *Actinomyces* bands showed an interesting trend on day 7, where *Actinomyces* occupied a lower proportion in the dental plaque on CTRL (Figure 8c-ii). As the CTRL plaque reached phase 3 on day 7, the portion of anaerobic bacteria such as *Porphyromonas* and *Fusobacterium* is considerable (Figure 8c-iii). Thus, the relative amount of

https://doi.org/10.1021/acsnano.0c10431
ACS Nano 2021, 15, 6811−6828

Actinomyces, mainly facultative bacteria, may be reduced (Figure 8d).

As shown in Figure 8e, the ATP bioluminescence produced by live bacteria on day 3 was *ca.* 35% lower in 50MPC/50SBMA. Unexpectedly, there was no statistically significant difference on day 7. Probably both the slow growth rates of anaerobic bacteria and an increase in the dead aerobic bacteria as the dental plaque matured lead to lower ATP production. These results are consistent with the previous study suggesting that the dental plaque biomass saturated on day 4.[53] Our results indicate that the APE ZPs inhibited dental plaque formation, as shown by low bioluminescence. In particular, the delayed dental plaque formation was more pronounced in the early stage of use.

Actually, *in vivo* mechanical stress from oral activities such as tongue movement and chewing could be the primary factors resulting in the clearance of 50MPC/50SBMA. For instance, the chewing force of beagles is high (*ca.* 3714 N).[55] In contrast, many *in vivo* studies have studied the antifouling polymers implanted on rats' backs to minimize the mechanical stress from spontaneous movement. In this study, the beagle behavior was not restrained, aside from the retainer fixation (Figure S15f), and mechanical stress increases as the animal size increases; thus the medium-sized dog model places the implanted medical device under harsher conditions than those found in traditional small animal (such as mice) models. Therefore, it is encouraging that *ca.* 80% antifouling performance was retained after 3 days of unrestricted use in the beagle model.

CONCLUSION

In this study, we constructed the cornerstone of APE for the futuristic functional ZPs. We conducted a multidisciplinary investigation of APE and synthesized the non-APE ZP (100MPC/0SBMA) and APE ZPs (80MPC/20SBMA and 50MPC/50SBMA). In detail, (i) specific parameters affecting the APE, (ii) strategies to obtain polymers exhibiting the APE, and (iii) the interrelationship between the APE and antifouling performance have been identified. The extraordinary ion-responsive actuation of APE ZPs effectively maximized the antifouling efficiency in biological environments from pilot test to *in vivo* application. Besides, the osmotic force and charge screening effects regulated the APE actuation. Thus, the researchers can synthesize the APE ZPs considering our findings as a guideline. Furthermore, the swelling and increased hydration under ionic solution would be the optimized cues to determine whether the ZPs are really exhibiting APE.

The antifouling of hydration shell is a less foulant-specific technology since it was rooted in the entropic loss. Thus, we expected that APE could be applied not only in the oral cavity but also other parts of the body containing different bacterial strands. In addition, we anticipated that APE could raise the futuristic potential of ZPs, an alternative to PEGylation, in biomedical applications (*e.g.*, antifouling coating, drug delivery systems). For example, considering the facile surface modification process and outstanding performance without cytotoxicity (Figure S16), we suggest that 50MPC/50SBMA could be used in a further clinical study by replacing the retainer once every 3 days.

MATERIALS AND METHODS

Synthesis and Immobilization of the Catecholic ATRP Initiator. Dopamine, α-bromoisobutyryl bromide (BiBB), *N,N*-dimethylformamide (DMF), triethylamine (TEA), and Tris buffer were purchased from Sigma-Aldrich (St. Louis. MO, USA). First, 2.61 mmol dopamine was placed in a round-bottomed flask and purged. The purged dopamine was dissolved in DMF. Then, BiBB was added to dopamine solution in a molar ratio of 2:1 (dopamine:BiBB). The reaction was triggered with TEA and conducted for 3 h under inert conditions. The product is the catecholic ATRP initiator. To immobilize the initiators, a mixture of synthesized initiators and 40 mM of pH 8.5 Tris buffer was introduced onto the O_2-plasma-treated substrate: silicon wafer, poly(methyl methacrylate) (PMMA), and polyethylene terephthalate (PETG). This step lasted 3 h, and the solution became dark brown during the process. After 3 h, the loosely attached ATRP initiators were washed with deionized water (DW) twice.

Surface Modification *via* SI-ARGET ATRP. We purchased sulfobetaine methacrylate (SBMA), 2-methacryloyloxyethyl phosphorylcholine (MPC), methanol, copper(II) bromide (CuBr2), 2,2′-bipyridine (bpy), and L-ascorbic acid from Sigma-Aldrich (St. Louis, MO, USA). The two monomers with various molar ratios were dissolved in DW/MeOH solvent, and the total concentration was fixed at 3 mM. The additives, $CuBr_2$ (1 mM) and bpy (2 mM), were then added, and the solution became slightly blue because of the formation of the $CuBr_2$-bpy complex. Finally, L-ascorbic acid (10 mM) was added to trigger the polymerization. After L-ascorbic acid had been dissolved, the solution became dark red. The dark red solution was added to the initiator-tethered substrate to initiate SI-ARGET ATRP. The polymerization process was conducted for 6 h under ambient conditions, and the dark red solution gradually took on a weak blue color. The residual solvent was removed by heating at 80 °C in a vacuum, and loosely attached polymers were removed by washing twice with DW. The ZPs were prepared by varying the ratios of feed monomers (Figure S1). Crucially, before polymerization, we ensured that there were no impurities in the monomers (Figure S3a). The substrates (*e.g.*, silicon wafer, QCM electrode, PMMA, PETG resin) were selected for the purpose of each experiment, and the polymerization process is the same as described above.

Characterization of Immobilized Initiators and ZPs. We performed Raman spectroscopy (XploRA PLUS, HORIBA, France) measurements to determine the optimal immobilization time and verify the uniform grafting of ZPs. The ZPs were anchored to the silicon wafer. For Raman measurements, the 10× microscope objective (numerical aperture = 0.25) and 532 nm laser were exploited. The grafting spectrometer was set at 1800 grating, and the confocal was 100 μm. The laser intensity at the sample point was *ca.* 75 mW, and laser spot size was 2.6 μm in diameter. A 520 cm^{-1} peak of the silicon wafer was the standard to calibrate prior to measurement. In order to obtain reliable data, the laser was exposed to the samples 30 s and repeated five times. For spatially mapping analysis, the pixel was 2.5 μm × 2.5 μm considering the laser spot size, and the total number of a pixel was 400. Thus, 2000 spectra were obtained for each sample.

An ellipsometer (alpha SE, Woollam, USA) was used to measure the thickness and refractive index. The angle of the light source was fixed to 70°, and the lab-made liquid cell was used to measure the wet thickness. The Cauchy model was applied to fit the dry ZPs. The Cauchy model or Bruggeman effective medium approximation model was applied for the hydrated ZPs. Empirically, the Bruggeman model was fitted well for the swollen ZPs.[56] Each measurement was repeated at least five times, and only results with a mean square error <1 were considered as reliable.

We conducted ^1H nuclear magnetic resonance (NMR; Avance III HD 300, Bruker Biospin, USA) measurements to determine the number-average molecular weight and mole fractions of the monomers (Figure S3c). The solvents were deuterium oxide (D_2O) or deuterated chloroform ($CDCl_3$).

The surface coverage after SI-ARGET ATRP was measured using a 5 MHz oscillation quartz crystal microbalance (QCM; QCM 200, SRS, USA). The frequency difference after SI-ARGET ATPR was measured using QCM. Then, the mass density of adsorbed polymers (*i.e.*, surface coverage, μg/cm^2) was calculated based on the Sauerbrey

https://doi.org/10.1021/acsnano.0c10431
ACS Nano 2021, 15, 6811−6828

equation, in detail; the overtone number was 1.0, then the relative constant was 18 ng/cm^2/Hz.[57]

X-ray photoelectron spectroscopy (XPS; K-ALPHA, Thermo Fisher Scientific, USA) measurements and contact angle goniometer (Smart Drop Standard, Femtobiomed, Korea) were also used for surface characterization. We used an electrophoretic light scattering spectrophotometer (ELS Z-1000, Otsuka Portal, Japan) to investigate the surface ζ-potential. Atomic force microscopy (AFM; NX-10, Park systems) was used to measure the root-mean-square roughness, and an additional indentation accessory at 0.20 μm s^{-1} was used for the nanomechanical measurements. Further, OriginPro (OriginLab Co., Northampton, USA) was used to fit the spectra with the Gaussian model.

Molecular Dynamics Simulation. All simulations were performed in GROMACS-2018.6[58] using the OPLS all-atom force field (FF) and the TIP4P water model.[59] The coordinates and FF parameters of the ZPs at different mole fractions of MPC and SBMA (1:0, 1:1, and 0:1) were generated using the LigParGen web server (http://zarbi.chem.yale.edu/ligpargen), where bond, angle, dihedral, and Lennard-Jones (LJ) OPLS parameters with 1.14*CM1A partial atomic charges were calculated.[60] To enhance the electrostatic accuracy, the partial charges of SBMA were assigned from the sulfobetaine model developed by Shao *et al.*,[61] and those of the headgroup of phosphatidylcholine in MPC were parametrized within the OPLS FF reported by Róg *et al.*[62]

The polymer layer, which consisted of 200 polymers (10 × 10 × 2; 100 polymers per leaflet) aligned with a 1 nm distance, was solvated with *ca.* 2.3 × 10^4 water molecules in a periodic box (10 nm/side) (Figure 3a). In addition, 98 or 655 Na^+ and Cl^- ions were introduced to produce concentrations of 0.154 or 1 M, respectively. The terminal groups (hydroxyl groups) of the polymers were position restrained with a force constant of 1.0 × 10^4 kJ mol^{-1} nm^{-2}. Further, the NVT ensemble was used to fix the grafting density of 1.0 nm^{-2} to mimic the experimental conditions. A temperature of 310 K was maintained by applying a velocity-rescaling thermostat.[63] A real space cutoff of 1 nm was applied for the LJ and Coulomb potentials with the inclusion of particle mesh Ewald summation for long-range electrostatics.[64] The LINCS algorithm was used to constrain the bond lengths.

To understand the extent of hydration, the number of hydrogen bonds between polymers and water molecules was calculated, as shown in Figure 3d. Herein, we assumed that a hydrogen-bonding interaction existed when the donor−acceptor distance was <0.35 nm, and the angle of hydrogen-donor−acceptor triplet was 30°.[65] Note that other criteria (distances from 0.3 to 0.4 nm and angles from 20° to 40°) produce similar qualitative trends, confirming that the analysis does not significantly depend on the distance and angle criteria.

Simulations were performed for 500 ns with a time step of 2 fs using computational facilities supported by the National Supercomputing Center with supercomputing resources, including technical support (KSC-2019-CRE-0011). The last 50 ns of the trajectories were used for analyses.

Visualization of Hydration Dynamics. To measure the water content, we used *in situ* QCM (QCM with an additional flow cell accessory), and the flow rate was maintained at 0.3 mL min^{-1}. In addition, we used Raman spectroscopy to measure the average number of hydrogen bonds per water molecule (N_{HB}). Prior to the Raman spectroscopy measurements, the ZPs on the silicon wafer were fully hydrated in DW for 6 h. Then, the bulk water was removed by slightly tilting the substrate toward the commercial absorbent. The experimental condition was identical to the protocol above.

Increasingly Harsh Antifouling Assays. *In Vitro Protein Adsorption.* We used the bovine serum albumin (BSA; Sigma-Aldrich, USA) as a model protein. First, we used *in situ* QCM to measure the amount of adsorbed BSA (in ng cm^{-2}). BSA was diluted to 1 mg mL^{-1} in aqueous 0.0, 0.154, or 1.0 M NaCl solutions, depending on the experimental conditions. For each measurement, the samples were saturated every step for 20 min for improved resolution. We also used the bicinchoninic acid assay (BCA; Thermo Fisher Scientific, USA), following the manufacturer's protocol. Briefly, the ZP-tethered silicon wafers (1 cm^2) were thoroughly washed in fresh DW. After the washing step, we prepared a 2 mg mL^{-1} BSA solution, which was diluted with fresh 1× phosphate-buffered saline (PBS; Gibco Life Technologies, USA). Then, the BSA solution was introduced to the prewashed samples and incubated for 6 h inside the cell incubator (37 °C in a 5% CO_2/95% air humidified atmosphere). Then, washing and the addition of bicinchoninic acid were carried out. After an additional 30 min of incubation, the amount of adsorbed protein (in μg/mL) was determined based on the absorbance (at 562 nm) of 100 μL purple-colored solution using a microplate reader (Epoch, BioTek Instruments, USA). Finally, the unit was converted into μg/cm^2 for the convenient comparison with Figure 5a.

In Vitro Bacterial Adhesion for Single Bacterial Models. *Staphylococcus aureus* (25923, ATCC, USA) and *Pseudomonas aeruginosa* (10145, ATCC, USA) were used as Gram-positive and Gram-negative bacteria, respectively. Both bacteria were cultured in tryptic soy broth (soybean-casein digest media; Becton Dickinson and Company, USA) media and incubated under aerobic conditions at 37 °C. Both bacteria were isolated from each bacterial suspension by centrifugation, and fresh medium was added to prepare two bacterial suspensions with optical density (OD) of 0.3 at 600 nm. A bacterial concentration corresponding to an OD 0.3 is representative of the strongly contaminated conditions before biofilm formation.

Pristine silicon wafers were used as the control (CTRL) group, and ZP-grafted silicon wafers were used as the experimental group, respectively. All samples were prepared with 1 cm × 1 cm (width × height) size and were sterilized by UV-irradiation for 15 min. The samples were placed in a 1 mL aliquot of previously prepared *S. aureus* and *P. aeruginosa* suspensions and incubated for 48 h at 37 °C in a 5% CO_2/95% air humidified atmosphere. Subsequently, all samples were transferred to new well-plates, and the excess bacterial solution was washed away with Dulbecco's phosphate-buffered saline (DPBS; Gibco BRL, USA) for staining. Following the washing steps, the air-dried samples were passed through a Bunsen flame 3−4 times with the bacterial side facing up. These fixed samples were incubated with 0.1% crystal violet (Sigma_Aldrich, USA) for 10 min at room temperature. Following the staining step, the samples were washed twice with DPBS to remove the residual dye. The stained samples were placed into 24-well plate and filled with 500 μL of 95% ethanol to dissolve the crystal violet stain. After the crystal violet had been dissolved in ethanol, 100 μL was transferred into each well of a 96-well plate in triplicates, and the absorbance at 570 nm was measured using a microplate reader (Epoch, BioTek Instruments, USA). The stained samples without the ethanol dissolution steps were used to obtain the images of the bacteria attached to the substrate using field-emission scanning electron microscopy (FE-SEM, JEOS, IT-500HR, USA). In addition, the thickness of the multilayers of bacteria was measure with a profilometer (Dektak 150, Veeco).

Ex Vivo Biofilm Formation by Multiple Microorganisms. Human saliva was collected from healthy adult donors who had no active caries or periodontal disease and had not taken antibiotics within 3 months. Participants did not brush teeth for 24 h and abstained from food/drink intake for at least 2 h before donating saliva. The saliva was collected from six individuals and mixed in equal proportions. Then, the mixed saliva was diluted in sterile glycerol to a concentration of 30% and stored at −80 °C for use as a biofilm model. The biofilm model was cultured in McBain medium supplemented with mucin (type II, porcine, gastric) (2.5 g L^{-1}), bacteriological peptone (2.0 g L^{-1}), tryptone (2.0 g L^{-1}), yeast extract (1.0 g L^{-1}), NaCl (0.35 g L^{-1}), KCl (0.2 g L^{-1}), $CaCl_2$ (0.2 g L^{-1}), cysteine hydrochloride (0.1 g L^{-1}), hemein (0.001 g L^{-1}), and vitamin K1 (0.0002 g L^{-1}) at 37 °C for 24 h. From the cultured medium, 1.5 mL of the bacterial solution was placed on the sample. After incubation for 8, 16, and 24 h, an additional 1.5 mL of bacterial solution was placed on the samples after each period. The biofilms were allowed to grow for a total of 48 h. The samples were stained with a live/dead bacterial viability kit (Molecular Probes, Eugene, OR, USA) using the method described earlier for bacterial staining. The biofilm was then visualized at five randomly chosen positions using confocal laser scanning microscopy (CLSM, LSM700, Carl Zeiss, Thornwood, NY, USA). Axially stacked biofilm images were captured,

https://doi.org/10.1021/acsnano.0c10431
ACS Nano 2021, 15, 6811−6828

and the thicknesses of the biofilms were calculated using the associated software (Zen, Carl Zeiss, Thornwood, NY, USA). Additionally, the COMSTAT plug-in (Technical University of Denmark, Kongens Lyngby, Denmark) in ImageJ (NIH, Bethesda, MA, USA) was used to determine the average biomass.

In Vivo Biofilm Formation by Multiple Microorganisms. Animal. Three male beagles aged 12−14 months and weighing 10−12 kg were housed in separate cages following the guidelines of institutional animal care and use committee of Kyung Hee University Medical Center. As a split-mouth design, both quadrants on maxillary and mandibular arches were randomly divided into two groups according to the retainer type: vacuum-formed retainers (VFRs) with or without 50MPC/50SBMA. The experimental protocols were approved by the ethics committee on animal research of Kyung Hee University (KHMC-IACUC 19−026) before the study commenced. The impression, insertion, and removal of clear retainers were nonsurgical procedures. For screw placement, sufficient local anesthesia was performed, and antibiotics and analgesics were administered for 3 days. Tissue regeneration occurred in the area where the screw was removed. There was no irreversible procedure such as tissue harvesting. The dog food was provided by grinding, body weight was measured, and scaling was performed once a week. After completing the experiment, the beagles were not sacrificed and were transferred to a Beagle Rescue Network, a nonprofit organization based in South Korea rescuing laboratory animals after experiments. We supported beagles' medical examination and neutralization processes. The further socialization process for adoption was undergone in the organization.

Fabrication of VFRs and Intraoral Experimental Protocols. After scaling and oral prophylaxis, the impression process was achieved using vinyl polysiloxane elastomeric silicone (3M Imprint II Garant Regular/Light Body VPS Impression Material, 3M, Minneapolis, US) (Figure S15a). The dental cast was fabricated using brownstone (GC FUJIROCK EP, GC America Inc., Illinois, US) (Figure S15b). Thermoplastic sheets composed of PETG with 1.0 mm thickness were used (Thermoforming Foil Track A; Forestadent, Pforzheim, Germany). The PETG sheets were vacuum-formed on the dental casts using a thermoforming machine (Track V; Forestadent, Pforzheim, Germany) according to the manufacturer's instructions (rated temperature, 160 °C; cooling period, 45 s). The VFRs covered the second, third, and fourth premolars and the first molar, and the margin was present at the gingival margin level (Figure S15c). The VFRs were delivered on the maxillary and mandibular arch and maintained intraorally for 3 and 7 days, respectively. To obtain sufficient retention, a hole with a 4 mm diameter was cut in the buccal surface of the first molar and the second premolar area in VFRs, and additional resin bonding was performed. After etching with 37% phosphoric acid on the enamel surface (Figure S15d), self-adhesive resin cement (RelyX Unicem Self-Adhesive Universal Resin Cement, 3M, Minneapolis, US) was used to attach the VFRs to the teeth (Figure S15e). To prevent the VFRs from falling out of the mouth, an orthodontic mini-implant (Jin-E Screw, Jin Biomed Co., Bucheon, Korea) was installed in the alveolar crest area between premolars (Figure S15f). All procedures were performed under general anesthesia by intramuscular injection of 4:1 combination of Zoletil 50 (0.15 mL kg^{-1}, Virbac Lab., Carros, France) and Rompun Inj. (0.15 mL kg^{-1}, Bayer Korea, Seoul, South Korea). After 3 or 7 days of intraoral use (Figure S15g), the VFRs were removed (Figure S15h). The used VFRs were cut into 4 mm × 6 mm-sized multiple rectangular pieces for the antifouling assays.

Scanning Electron Microscopy (SEM). In a previous study using pyrosequencing, initial bacterial colonizers were detected in canine dental plaque formed for 1−2 days. However, sufficient bacterial biofilm was not formed on the specimen surfaces up to 2 days in our preliminary experiments (data not shown). Hence, in this study, we maintained the specimens in beagle oral cavities for 3 or 7 days for subsequent observation of the biofilms by SEM. Each specimen was removed from the oral cavity and washed gently with physiological saline three times, and the biofilms were fixed for 1 h with 2.5% (wt/vol) glutaraldehyde prepared in a filter-sterilized phosphate buffer (0.1 M; pH 7.4) and then rinsed three times with distilled water. The biofilms were postfixed for 1 h with 1% (wt/vol) osmium tetroxide in 0.1 M phosphate buffer, followed by a quick rinse in distilled water. The fixed biofilms were dehydrated in successive ethanol-water mixtures with increasing ethanol concentrations of 25%, 50%, and 75% by volume for 10 min each and then twice in pure ethanol for 10 min each. The biofilm samples were dried by critical point drying and then coated with gold using a sputter coater (IB-3; Eiko, Tokyo, Japan). The bacterial biofilms formed on the inner (covering the teeth) and outer surfaces (contacting the opposing teeth) of the specimens were observed by SEM (model S-4700; Hitachi High Technologies America, Inc., Pleasanton, CA) at 10 kV.

Bacterial ATP Bioluminescence Assay. To compare the difference in activities of live bacteria on the surface of each specimen, bacterial ATP was measured using the BacTiter-Glo viability assay kit (Promega, Madison, WI, USA) according to the manufacturer's instructions. The luminescence signals were recorded using a Dynex Triad multimode plate reader (Dynex Technologies, Chantilly, VA, USA) and expressed as relative luminescence units (RLU) normalized to the surface area of the sample (RLU mm^{-2}).

DNA Isolation and Polymerase Chain Reaction. *Actinomyces*, *Porphyromonas*, and *Neisseria* are known to be major bacterial genera present in the human as well as canine oral microbiome. To compare the amount of DNA derived from the members of these three bacterial genera present in the biofilms, polymerase chain reaction (PCR) was performed using genus-specific primers (Table S4).[66] According to the manufacturer's instructions, the bacterial genomic DNA was extracted from each specimen divided into small pieces, using Instagene Matrix (Bio-Rad, Hercules, CA, USA). Briefly, the supernatant (300 μL) containing bacterial DNA was obtained from a specimen piece of the same area, 2 μL of which was used as a template in each reaction. PCR amplification was performed in a total volume of 20 μL containing AccuPowerPCR PreMix (Bioneer, Daejeon, Korea) with 0.5 μM of each primer and 2 μL of the template DNA. PCR conditions: initial denaturation at 95 °C for 5 min, 20 cycles of denaturation at 95 °C for 20 s, annealing at 57 °C for 20 s, extension at 72 °C for 30 s, and a final extension at 72 °C for 5 min. PCR products (10 μL) were separated by electrophoresis on 2.0% agarose gels in TBE buffer (89 mM Tris-borate, 2 mM EDTA, pH 8.0) and then observed under UV trans-illuminator (Bio-Rad). The intensity of DNA bands was analyzed using ImageJ.

Cytotoxicity Tests. The ZPs were anchored to the surface as mentioned above. Thus, the grafting density would be the same in Table S1. The cytotoxicity of the synthesized ZPs was evaluated, using human dermal fibroblast (HDF; CC-2511, Lonza, Switzerland) cells as model cells. The cells were fully activated until passage no. 9 by incubation at 37 °C in a humidified incubator in 5% CO_2 in Dulbecco's modified Eagle medium supplemented with 10% fetal bovine serum (FBS; Gibco Life Technologies, USA). The prewashed samples were placed in a 24-well cell culture plate, and the cells were seeded with a density of 3.0×10^4 cells mL^{-1}. After 24 h incubation, we conducted both Cell Counting Kit (CCK) assay (D-Plus CCK cell viability assay kit, Dongin LS, Korea) and counter-staining following the manufacturer's protocol. Briefly, each well was treated with CCK assay solution and incubated for 1 h. The relative number of viable cells was measured based on the optical density at 450 nm. On the other hand, for counter-staining, we first stained the cytoplasm with 5 μM 5-chloromethylfluorescein diacetate (CellTracker Green CMFDA, Thermo Fisher Scientific, USA) for 30 min. Then, the green-stained cells were fixed with 4% formaldehyde (Sigma-Aldrich, USA) for approximately 15 min at ambient temperature. The nuclei were stained blue with 300 nM 4′,6-diamidino-2-phenylindole (DAPI; Thermo Fisher Scientific, USA). The excitation and emission wavelengths of the two dyes were significantly different. Thus, the counter-stained images were obtained using fluorescence microscope (IX51, Olympus), and images were merged using ImageJ.

Statistical Analysis. In Figures 5−7, we conducted Student's *t* test to individually evaluate the significant antifouling performance of 50MPC/50SBMA than the control, non-APE ZP (100MPC/0SBMA), and weakly APE ZPs (80MPC/20SBMA). In Figure S16,

https://doi.org/10.1021/acsnano.0c10431
ACS Nano 2021, 15, 6811−6828

we conducted the one-way ANOVA to show that all ZPs are not cytotoxic. The symbols * (P-value < 0.05), ** (P-value < 0.01), and *** (P-value < 0.001) indicated the statistical significance.

ASSOCIATED CONTENT

Supporting Information

The Supporting Information is available free of charge at https://pubs.acs.org/doi/10.1021/acsnano.0c10431.

Figures S1−S16 and Tables S1−S4 (PDF)

Movie S1: Superhydrophilicity of 100MPC/0SBMA (MP4)

Movie S2: Superhydrophilicity of 80MPC/20SBMA (MP4)

Movie S3: Superhydrophilicity of 50MPC/50SBMA (MP4)

Movie S4: Non-gel-like structure of 50MPC/50MPC (MP4)

Movie S5: Gel-like structure of 0MPC/100SBMA (MP4)

AUTHOR INFORMATION

Corresponding Authors

Jinkee Hong − *Department of Chemical and Biomolecular Engineering, College of Engineering, Yonsei University, Seoul 03722, Republic of Korea;* orcid.org/0000-0003-3243-8536; Email: jinkee.hong@yonsei.ac.kr

Hyo-Won Ahn − *Department of Orthodontics, School of Dentistry, Kyung Hee University, Seoul 02447, Republic of Korea*; Email: hyowon@khu.ac.kr

Hwankyu Lee − *Department of Chemical Engineering, Dankook University, Yongin-si, Gyeonggi-do 16890, Republic of Korea;* orcid.org/0000-0002-2036-1490; Email: leeh@dankook.ac.kr

Sung-Hwan Choi − *Department of Orthodontics, Institute of Craniofacial Deformity and BK21 FOUR Project, Yonsei University College of Dentistry, Seoul 03722, Republic of Korea;* orcid.org/0000-0002-1150-0268; Email: selfexam@yuhs.ac

Authors

Woojin Choi − *Department of Chemical and Biomolecular Engineering, College of Engineering, Yonsei University, Seoul 03722, Republic of Korea;* orcid.org/0000-0002-5886-8836

Sohyeon Park − *Department of Chemical and Biomolecular Engineering, College of Engineering, Yonsei University, Seoul 03722, Republic of Korea*

Jae-Sung Kwon − *Department and Research Institute of Dental Biomaterials and Bioengineering and BK21 FOUR Project, Yonsei University College of Dentistry, Seoul 03722, Republic of Korea;* orcid.org/0000-0001-9803-7730

Eun-Young Jang − *Department of Dentistry, Graduate School, Kyung Hee University, Seoul 02447, Republic of Korea*

Ji-Yeong Kim − *Department of Orthodontics, Institute of Craniofacial Deformity and BK21 FOUR Project, Yonsei University College of Dentistry, Seoul 03722, Republic of Korea*

Jiwoong Heo − *Department of Chemical and Biomolecular Engineering, College of Engineering, Yonsei University, Seoul 03722, Republic of Korea*

YoungDeok Hwang − *Paul H. Chook Department of Information Systems and Statistics, Baruch College CUNY, New York 10010, United States*

Byeong-Su Kim − *Department of Chemistry, Yonsei University, Seoul 03722, Republic of Korea;* orcid.org/0000-0002-6419-3054

Ji-Hoi Moon − *Department of Oral Microbiology, School of Dentistry, Kyung Hee University, Seoul 02447, Republic of Korea*

Sungwon Jung − *Department of Chemical and Biomolecular Engineering, College of Engineering, Yonsei University, Seoul 03722, Republic of Korea*

Complete contact information is available at: https://pubs.acs.org/10.1021/acsnano.0c10431

Notes

The authors declare no competing financial interest.

ACKNOWLEDGMENTS

J.H. acknowledges funding from the National Research Foundation of Korea (NRF) funded by the Ministry of Science and ICT (NRF-2017R1E1A1A01074343), Bio and Medical Technology Development Program of the National Research Foundation (NRF) funded by the Ministry of Science and ICT (2016M3A9C6917405, 2019M3A9H110378611), Korea Medical Device Development Fund grant funded by the Korea government (the Ministry of Science and ICT, the Ministry of Trade, Industry and Energy, the Ministry of Health and Welfare, Republic of Korea, the Ministry of Food and Drug Safety) (project number: 202011D04), and Samsung (SRFC-MA1602-07). H.-W.A. acknowledges funding from the National Research Foundation of Korea (NRF) grant funded by the Korea government (MSIT) (NRF-2019R1F1A1042263). H.L. acknowledges funding from the Basic Science Research Program through the National Research Foundation of Korea (NRF) funded by the Ministry of Science and ICT (NRF-2017R1D1A1A09000510). S.-H.C. acknowledges funding from the Basic Science Research Program through the National Research Foundation of Korea (NRF) and funded by the Ministry of Science, ICT and Future Planning (NRF-2018R1C1B6000989). B.-S.K. acknowledges funding from the Samsung (SRFC-MA1602-07).

REFERENCES

(1) Francolini, I.; Donelli, G. Prevention and Control of Biofilm-Based Medical-Device-Related Infections. *FEMS Immunol. Med. Microbiol.* **2010**, *59*, 227−238.

(2) Van Doremalen, N.; Bushmaker, T.; Morris, D. H.; Holbrook, M. G.; Gamble, A.; Williamson, B. N.; Tamin, A.; Harcourt, J. L.; Thornburg, N. J.; Gerber, S. I. Aerosol and Surface Stability of Sars-Cov-2 as Compared with Sars-Cov-1. *N. Engl. J. Med.* **2020**, *382*, 1564−1567.

(3) Ding, X.; Yang, C.; Lim, T. P.; Hsu, L. Y.; Engler, A. C.; Hedrick, J. L.; Yang, Y.-Y. Antibacterial and Antifouling Catheter Coatings Using Surface Grafted Peg-B-Cationic Polycarbonate Diblock Copolymers. *Biomaterials* **2012**, *33*, 6593−6603.

(4) Hatakeyama, H.; Akita, H.; Harashima, H. The Polyethyleneglycol Dilemma: Advantage and Disadvantage of Pegylation of Liposomes for Systemic Genes and Nucleic Acids Delivery to Tumors. *Biol. Pharm. Bull.* **2013**, *36*, 892−899.

(5) Knop, K.; Hoogenboom, R.; Fischer, D.; Schubert, U. S. Poly (Ethylene Glycol) in Drug Delivery: Pros and Cons as Well as Potential Alternatives. *Angew. Chem., Int. Ed.* **2010**, *49*, 6288−6308.

(6) Estephan, Z. G.; Schlenoff, P. S.; Schlenoff, J. B. Zwitteration as an Alternative to Pegylation. *Langmuir* **2011**, *27*, 6794−6800.

(7) Keefe, A. J.; Jiang, S. Poly (Zwitterionic) Protein Conjugates Offer Increased Stability without Sacrificing Binding Affinity or Bioactivity. *Nat. Chem.* **2012**, *4*, 59−63.
(8) Erathodiyil, N.; Chan, H.-M.; Wu, H.; Ying, J. Y. Zwitterionic Polymers and Hydrogels for Antibiofouling Applications in Implantable Devices. *Mater. Today* **2020**, *38*, 84−98.
(9) Wu, J.; Lin, W.; Wang, Z.; Chen, S.; Chang, Y. Investigation of the Hydration of Nonfouling Material Poly (Sulfobetaine Methacrylate) by Low-Field Nuclear Magnetic Resonance. *Langmuir* **2012**, *28*, 7436−7441.
(10) Schlenoff, J. B. Zwitteration: Coating Surfaces with Zwitterionic Functionality to Reduce Nonspecific Adsorption. *Langmuir* **2014**, *30*, 9625−9636.
(11) Xiao, S.; Zhang, Y.; Shen, M.; Chen, F.; Fan, P.; Zhong, M.; Ren, B.; Yang, J.; Zheng, J. Structural Dependence of Salt-Responsive Polyzwitterionic Brushes with an Anti-Polyelectrolyte Effect. *Langmuir* **2018**, *34*, 97−105.
(12) Xiao, S.; Ren, B.; Huang, L.; Shen, M.; Zhang, Y.; Zhong, M.; Yang, J.; Zheng, J. Salt-Responsive Zwitterionic Polymer Brushes with Anti-Polyelectrolyte Property. *Curr. Opin. Chem. Eng.* **2018**, *19*, 86−93.
(13) Zhang, Y.; Liu, Y.; Ren, B.; Zhang, D.; Xie, S.; Chang, Y.; Yang, J.; Wu, J.; Xu, L.; Zheng, J. Fundamentals and Applications of Zwitterionic Antifouling Polymers. *J. Phys. D: Appl. Phys.* **2019**, *52*, 403001.
(14) Xiao, S.; He, X.; Zhao, Z.; Huang, G.; Yan, Z.; He, Z.; Zhao, Z.; Chen, F.; Yang, J. Strong Anti-Polyelectrolyte Zwitterionic Hydrogels with Superior Self-Recovery, Tunable Surface Friction, Conductivity, and Antifreezing Properties. *Eur. Polym. J.* **2021**, *148*, 110350.
(15) Huang, K.-T.; Ishihara, K.; Huang, C.-J. Polyelectrolyte and Antipolyelectrolyte Effects for Dual Salt-Responsive Interpenetrating Network Hydrogels. *Biomacromolecules* **2019**, *20*, 3524−3534.
(16) Chen, H.; Yang, J.; Xiao, S.; Hu, R.; Bhaway, S. M.; Vogt, B. D.; Zhang, M.; Chen, Q.; Ma, J.; Chang, Y. Salt-Responsive Polyzwitterionic Materials for Surface Regeneration between Switchable Fouling and Antifouling Properties. *Acta Biomater.* **2016**, *40*, 62−69.
(17) Zhang, Z.; Moxey, M.; Alswieleh, A.; Morse, A. J.; Lewis, A. L.; Geoghegan, M.; Leggett, G. J. Effect of Salt on Phosphorylcholine-Based Zwitterionic Polymer Brushes. *Langmuir* **2016**, *32*, 5048−5057.
(18) Han, D.; Letteri, R.; Chan-Seng, D.; Emrick, T.; Tu, H. Examination of Zwitterionic Polymers and Gels Subjected to Mechanical Constraints. *Polymer* **2013**, *54*, 2887−2894.
(19) Shao, Q.; Jiang, S. Molecular Understanding and Design of Zwitterionic Materials. *Adv. Mater.* **2015**, *27*, 15−26.
(20) Georgiev, G. S.; Kamenska, E. B.; Vassileva, E. D.; Kamenova, I. P.; Georgieva, V. T.; Iliev, S. B.; Ivanov, I. A. Self-Assembly, Antipolyelectrolyte Effect, and Nonbiofouling Properties of Polyzwitterions. *Biomacromolecules* **2006**, *7*, 1329−1334.
(21) Jiang, S.; Cao, Z. Ultralow-Fouling, Functionalizable, and Hydrolyzable Zwitterionic Materials and Their Derivatives for Biological Applications. *Adv. Mater.* **2010**, *22*, 920−932.
(22) Fristrup, C. J.; Jankova, K.; Hvilsted, S. Surface-Initiated Atom Transfer Radical Polymerization—A Technique to Develop Biofunctional Coatings. *Soft Matter* **2009**, *5*, 4623−4634.
(23) Lee, H.; Dellatore, S. M.; Miller, W. M.; Messersmith, P. B. Mussel-Inspired Surface Chemistry for Multifunctional Coatings. *Science* **2007**, *318*, 426−430.
(24) Hong, D.; Bae, K.; Hong, S.-P.; Park, J. H.; Choi, I. S.; Cho, W. K. Mussel-Inspired, Perfluorinated Polydopamine for Self-Cleaning Coating on Various Substrates. *ChemComm* **2014**, *50*, 11649−11652.
(25) Rocha, W.; Pilling, S. Determination of Optical Constants N and K of Thin Films from Absorbance Data Using Kramers-Kronig Relationship. *Spectrochim. Acta, Part A* **2014**, *123*, 436−446.
(26) Kim, J. Y.; Lee, B. S.; Choi, J.; Kim, B. J.; Choi, J. Y.; Kang, S. M.; Yang, S. H.; Choi, I. S. Cytocompatible Polymer Grafting from Individual Living Cells by Atom-Transfer Radical Polymerization. *Angew. Chem., Int. Ed.* **2016**, *55*, 15306−15309.
(27) Yang, Y.; Yan, X.; Cui, Y.; He, Q.; Li, D.; Wang, A.; Fei, J.; Li, J. Preparation of Polymer-Coated Mesoporous Silica Nanoparticles Used for Cellular Imaging by a "Graft-From" Method. *J. Mater. Chem.* **2008**, *18*, 5731−5737.
(28) Li, D.; He, Q.; Yang, Y.; Möhwald, H.; Li, J. Two-Stage pH Response of Poly (4-Vinylpyridine) Grafted Gold Nanoparticles. *Macromolecules* **2008**, *41*, 7254−7256.
(29) Brault, N. D.; Sundaram, H. S.; Li, Y.; Huang, C.-J.; Yu, Q.; Jiang, S. Dry Film Refractive Index as an Important Parameter for Ultra-Low Fouling Surface Coatings. *Biomacromolecules* **2012**, *13*, 589−593.
(30) Khan, M. O.; Åkesson, T.; Jönsson, B. Adsorption of Polyampholytes to Charged Surfaces. *Macromolecules* **2001**, *34*, 4216−4221.
(31) Hochella Jr, M.; Carim, A. A Reassessment of Electron Escape Depths in Silicon and Thermally Grown Silicon Dioxide Thin Films. *Surf. Sci.* **1988**, *197*, L260−L268.
(32) Li, D.; Wei, Q.; Wu, C.; Zhang, X.; Xue, Q.; Zheng, T.; Cao, M. Superhydrophilicity and Strong Salt-Affinity: Zwitterionic Polymer Grafted Surfaces with Significant Potentials Particularly in Biological Systems. *Adv. Colloid Interface Sci.* **2020**, *278*, 102141.
(33) Blackman, L. D.; Gunatillake, P. A.; Cass, P.; Locock, K. E. An Introduction to Zwitterionic Polymer Behavior and Applications in Solution and at Surfaces. *Chem. Soc. Rev.* **2019**, *48*, 757−770.
(34) Kobayashi, M.; Terayama, Y.; Kikuchi, M.; Takahara, A. Chain Dimensions and Surface Characterization of Superhydrophilic Polymer Brushes with Zwitterion Side Groups. *Soft Matter* **2013**, *9*, 5138−5148.
(35) Kudaibergenov, S. E.; Nuraje, N. Intra-and Interpolyelectrolyte Complexes of Polyampholytes. *Polymers* **2018**, *10*, 1146.
(36) Javanainen, M.; Melcrová, A.; Magarkar, A.; Jurkiewicz, P.; Hof, M.; Jungwirth, P.; Martinez-Seara, H. Two Cations, Two Mechanisms: Interactions of Sodium and Calcium with Zwitterionic Lipid Membranes. *ChemComm* **2017**, *53*, 5380−5383.
(37) Shusharina, N.; Zhulina, E.; Dobrynin, A.; Rubinstein, M. Scaling Theory of Diblock Polyampholyte Solutions. *Macromolecules* **2005**, *38*, 8870−8881.
(38) Wang, T.-Y.; Lee, T.-R.; Sheng, Y.-J.; Tsao, H.-K. Effective Charges of Polyelectrolytes in a Salt-Free Solution Based on Counterion Chemical Potential. *J. Phys. Chem. B* **2005**, *109*, 22560−22569.
(39) Wang, F.; Yang, J.; Zhao, J. Understanding Anti-Polyelectrolyte Behavior of a Well-Defined Polyzwitterion at the Single-Chain Level. *Polym. Int.* **2015**, *64*, 999−1005.
(40) Shao, Q.; He, Y.; Jiang, S. Molecular Dynamics Simulation Study of Ion Interactions with Zwitterions. *J. Phys. Chem. B* **2011**, *115*, 8358−8363.
(41) Cera, L.; Gonzalez, G. M.; Liu, Q.; Choi, S.; Chantre, C. O.; Lee, J.; Gabardi, R.; Choi, M. C.; Shin, K.; Parker, K. K. A Bioinspired and Hierarchically Structured Shape-Memory Material. *Nat. Mater.* **2021**, *20*, 242−249.
(42) Dai, W.; Zheng, C.; Zhao, B.; Chen, K.; Jia, P.; Yang, J.; Zhao, J. A Negative Correlation between Water Content and Protein Adsorption on Polymer Brushes. *J. Mater. Chem. B* **2019**, *7*, 2162−2168.
(43) Sun, Q. Raman Spectroscopic Study of the Effects of Dissolved Nacl on Water Structure. *Vib. Spectrosc.* **2012**, *62*, 110−114.
(44) Choi, W.; Jin, J.; Park, S.; Kim, J.-Y.; Lee, M.-J.; Sun, H.; Kwon, J.-S.; Lee, H.; Choi, S.-H.; Hong, J. Quantitative Interpretation of Hydration Dynamics Enabled the Fabrication of a Zwitterionic Antifouling Surface. *ACS Appl. Mater. Interfaces* **2020**, *12*, 7951−7965.
(45) Chen, H.; Zhang, M.; Yang, J.; Zhao, C.; Hu, R.; Chen, Q.; Chang, Y.; Zheng, J. Synthesis and Characterization of Antifouling Poly (N-Acryloylaminoethoxyethanol) with Ultralow Protein Adsorption and Cell Attachment. *Langmuir* **2014**, *30*, 10398−10409.
(46) Cao, Z.; Casabona, M. G.; Kneuper, H.; Chalmers, J. D.; Palmer, T. The Type Vii Secretion System of *Staphylococcus aureus* Secretes a Nuclease Toxin That Targets Competitor Bacteria. *Nat. Microbiol.* **2017**, *2*, 16183.

https://doi.org/10.1021/acsnano.0c10431
ACS Nano 2021, 15, 6811−6828

(47) Hauser, A. R. The Type Iii Secretion System of Pseudomonas Aeruginosa: Infection by Injection. *Nat. Rev. Microbiol.* **2009**, *7*, 654−665.
(48) Park, S.; Kim, H.-h.; Yang, S. B.; Moon, J.-H.; Ahn, H.-W.; Hong, J. A Polysaccharide-Based Antibacterial Coating with Improved Durability for Clear Overlay Appliances. *ACS Appl. Mater. Interfaces* **2018**, *10*, 17714−17721.
(49) Quirynen, M.; Bollen, C. The Influence of Surface Roughness and Surface-Free Energy on Supra-and Subgingival Plaque Formation in Man: A Review of the Literature. *J. Clin. Periodontol.* **1995**, *22*, 1−14.
(50) Rumbaugh, K. P.; Sauer, K. Biofilm Dispersion. *Nat. Rev. Microbiol.* **2020**, *18*, 571−586.
(51) Otto, M. Staphylococcal Infections: Mechanisms of Biofilm Maturation and Detachment as Critical Determinants of Pathogenicity. *Annu. Rev. Med.* **2013**, *64*, 175−188.
(52) Filoche, S.; Wong, L.; Sissons, C. Oral Biofilms: Emerging Concepts in Microbial Ecology. *J. Dent. Res.* **2010**, *89*, 8−18.
(53) Takeshita, T.; Yasui, M.; Shibata, Y.; Furuta, M.; Saeki, Y.; Eshima, N.; Yamashita, Y. Dental Plaque Development on a Hydroxyapatite Disk in Young Adults Observed by Using a Barcoded Pyrosequencing Approach. *Sci. Rep.* **2015**, *5*, 8136.
(54) Holcombe, L. J.; Patel, N.; Colyer, A.; Deusch, O.; O'Flynn, C.; Harris, S. Early Canine Plaque Biofilms: Characterization of Key Bacterial Interactions Involved in Initial Colonization of Enamel. *PLoS One* **2014**, *9*, No. e113744.
(55) Thomason, J. Cranial Strength in Relation to Estimated Biting Forces in Some Mammals. *Can. J. Zool.* **1991**, *69*, 2326−2333.
(56) Daniel, D.; Chia, A. Y. T.; Moh, L. C. H.; Liu, R.; Koh, X. Q.; Zhang, X.; Tomczak, N. Hydration Lubrication of Polyzwitterionic Brushes Leads to Nearly Friction-and Adhesion-Free Droplet Motion. *Commun. Phys.* **2019**, *2*, 105.
(57) Jones, O. G.; Mezzenga, R. Inhibiting, Promoting, and Preserving Stability of Functional Protein Fibrils. *Soft Matter* **2012**, *8*, 876−895.
(58) Lindahl, E.; Hess, B.; Van Der Spoel, D. Gromacs 3.0: A Package for Molecular Simulation and Trajectory Analysis. *J. Mol. Model.* **2001**, *7*, 306−317.
(59) Kaminski, G. A.; Friesner, R. A.; Tirado-Rives, J.; Jorgensen, W. L. Evaluation and Reparametrization of the Opls-Aa Force Field for Proteins *via* Comparison with Accurate Quantum Chemical Calculations on Peptides. *J. Phys. Chem. B* **2001**, *105*, 6474−6487.
(60) Dodda, L. S.; Vilseck, J. Z.; Tirado-Rives, J.; Jorgensen, W. L. 1.14* Cm1a-Lbcc: Localized Bond-Charge Corrected Cm1a Charges for Condensed-Phase Simulations. *J. Phys. Chem. B* **2017**, *121*, 3864−3870.
(61) Shao, Q.; He, Y.; White, A. D.; Jiang, S. Difference in Hydration between Carboxybetaine and Sulfobetaine. *J. Phys. Chem. B* **2010**, *114*, 16625−16631.
(62) Kulig, W.; Pasenkiewicz-Gierula, M.; Róg, T. opologies, structures and parameter files for lipid simulations in GROMACS with the OPLS-aa force field: DPPC, POPC, DOPC, PEPC, and cholesterol. *Data in Brief* **2015**, *5*, 333−336.
(63) Bussi, G.; Donadio, D.; Parrinello, M. Canonical Sampling through Velocity Rescaling. *J. Chem. Phys.* **2007**, *126*, 014101.
(64) Essmann, U.; Perera, L.; Berkowitz, M. L.; Darden, T.; Lee, H.; Pedersen, L. G. A Smooth Particle Mesh Ewald Method. *J. Chem. Phys.* **1995**, *103*, 8577−8593.
(65) Jeffrey, G. A., Saenger, W. Theoretical Calculations of Hydrogen-Bond Geometries. In *Hydrogen Bonding in Biological Structures*; Springer Science & Business Media: Berlin, Heidelberg, 2012; pp 71−93.
(66) Sun, B.; Zhou, D.; Tu, J.; Lu, Z. Evaluation of the Bacterial Diversity in the Human Tongue Coating Based on Genus-Specific Primers for 16s rRNA Sequencing. *BioMed. Res. Int.* **2017**, *2017*, 8184160.

https://doi.org/10.1021/acsnano.0c10431
ACS Nano 2021, 15, 6811−6828